

Structural mechanism of anti-MHC-I antibody blocking of inhibitory NK cell receptors in tumor immunity

Received: 6 August 2025

Accepted: 22 January 2026

Cite this article as: Jiang, J., Panda, A.K., Natarajan, K. *et al.* Structural mechanism of anti-MHC-I antibody blocking of inhibitory NK cell receptors in tumor immunity.

Commun Biol (2026). <https://doi.org/10.1038/s42003-026-09641-8>

Jiansheng Jiang, Abir K. Panda, Kannan Natarajan, Haotian Lei, Shikha Sharma, Lisa F. Boyd, Reanne R. Towler, Sruthi Chempati, Javeed Ahmad, Abraham J. Morton, Zabrina C. Lang, Yi Sun, Nikolaos Sgourakis, Martin Meier-Schellersheim, Rick K. Huang, Ethan M. Shevach & David H. Margulies

We are providing an unedited version of this manuscript to give early access to its findings. Before final publication, the manuscript will undergo further editing. Please note there may be errors present which affect the content, and all legal disclaimers apply.

If this paper is publishing under a Transparent Peer Review model then Peer Review reports will publish with the final article.

Structural mechanism of anti-MHC-I antibody blocking of inhibitory NK cell receptors in tumor immunity

Jiansheng Jiang^{1*§}, Abir K. Panda^{2*}, Kannan Natarajan^{1*}, Haotian Lei³, Shikha Sharma⁴, Lisa F. Boyd¹, Reanne R. Towler¹, Sruthi Chempati², Javeed Ahmad^{1,5} Abraham J. Morton⁶, Zabrina C. Lang⁶, Yi Sun⁷, Nikolaos Sgourakis⁷, Martin Meier-Schellersheim⁴, Rick K. Huang⁶, Ethan M. Shevach², and David H. Margulies^{1,§}

* These authors contributed equally

§ corresponding authors (jiangji@niaid.nih.gov, eshevach@niaid.nih.gov, dmargulies@niaid.nih.gov)

¹Molecular Biology Section, Laboratory of Immune System Biology, National Institute of Allergy and Infectious Diseases, National Institutes of Health, Bethesda, MD, 20892, USA

²Cellular Immunology Section, Laboratory of Immune System Biology, National Institute of Allergy and Infectious Diseases, National Institutes of Health, Bethesda, MD, 20892, USA

³Research Technology Branch, National Institute of Allergy and Infectious Diseases, National Institutes of Health, Bethesda, MD, 20892, USA

⁴Computational Systems Biology Section, Laboratory of Immune System Biology, National Institute of Allergy and Infectious Diseases, National Institutes of Health, Bethesda, MD, 20892, USA

⁵Fred and Pamela Buffett Cancer Center and Eppley Institute for Cancer Research, Omaha, NE, 68198, USA

⁶Laboratory of Cell Biology, Center for Cancer Research, National Cancer Institute, Bethesda, MD, 20892, USA

⁷Perelman School of Medicine, University of Pennsylvania, Philadelphia, PA, USA

ABSTRACT

Anti-major histocompatibility complex class I (MHC-I) mAbs can stimulate immune responses to tumors and infections by blocking suppressive signals delivered via various immune inhibitory receptors. To understand such functions, we determined the structure of a highly cross-reactive anti-human MHC-I mAb, B1.23.2, in complex with the MHC-I molecule HLA-B*44:05 by both cryo-electron microscopy (cryo-EM) and X-ray crystallography. Structural models determined by the two methods were essentially identical revealing that B1.23.2 binds a conserved region on the $\alpha 2_1$ helix that overlaps the killer immunoglobulin-like receptor (KIR) binding site. Structural comparison to KIR/HLA complexes reveals a mechanism by which B1.23.2 blocks inhibitory receptor interactions, leading to natural killer (NK) cell activation. B1.23.2 treatment of the human KLM-1 pancreatic cancer model in humanized (NSG-IL15) mice provides evidence of suppression of tumor growth. Such anti-MHC-I mAb that block inhibitory KIR/HLA interactions may prove useful for tumor immunotherapy.

INTRODUCTION

MHC-I molecules, expressed on virtually all vertebrate somatic cells, play crucial roles in determining immunological and inflammatory responses to cancerous transformation and infection¹. Classical MHC-I molecules, designated HLA-A, -B, and -C in the human, bind peptides and display peptide/MHC-I (pMHC) complexes at the cell surface for recognition by activating or inhibitory receptors on natural killer (NK) cells, monocytes, and T cells². In humans, receptors expressed on NK cells and monocytes include killer immunoglobulin-like receptors (KIR) and leukocyte immunoglobulin-like receptors (LILRs or LIRs, also known as immunoglobulin-like transcripts (ILT))^{3,4}. Although KIR/HLA interactions exhibit a wide range of peptide preferences^{5,6}, and LILRs bind with little peptide discrimination^{7,8}, these interactions contrast with the exquisite peptide and MHC-I specificity exhibited by clonotypically variable T cell receptors (TCR)^{9,10}. MAbs to MHC-I have been used extensively to characterize the function and polymorphism of this family of cell surface molecules and may also activate immune responses to tumors and infections by blocking interactions with MHC-I binding inhibitory receptors¹¹⁻¹³.

Natural Killer (NK) cells play an important role in innate immunity against cancer and virus-infected cells¹⁴⁻¹⁶. NK cell function is regulated by activation and inhibitory receptors. Inhibitory receptors, such as KIR2DL and KIR3DL in the human or Ly49A and Ly49C in the mouse, recognize classical MHC-I (HLA or H2) molecules^{4,17,18}. Inhibition of NK activity through signals conveyed by MHC-I/inhibitory receptor interactions maintains homeostasis, while loss of such signals either through reduced expression of MHC-I on tumor cells (so-called “missing self”¹⁹) or by antibody masking^{11,12,20} leads to NK cell activation. Numerous X-ray crystal structures of various NK receptors (KIR, Ly49) or receptors expressed on a wide spectrum of

immune cells (such as LILR) alone, or in complex with MHC-I, have refined our understanding of the nature of recognition by these innate immune surface molecules^{18,21,22}. A variety of anti-receptor antibodies that block KIR/MHC-I or LILR/MHC-I inhibitory signals and thus activate innate immunity have been under development as cancer immunotherapies²³⁻²⁷, administered either alone or in combination with antibodies that relieve checkpoint inhibition²⁸.

Functional studies of two pan anti-human-MHC-I mAbs DX17 and W6/32²⁹ and X-ray crystal structures of these in complex with representative HLA ligands^{29,30} provided an understanding of their ability to block the binding and tonic inhibition contributed by the interaction of inhibitory receptors such as LILRB1 with MHC-I. We recently observed that another anti-human-MHC-I mAb, B1.23.2^{31,32}, also binds a wide range of human HLA-A, -B, and -C molecules. Cross-blocking experiments suggest that B1.23.2 functions to inhibit KIR interactions with MHC-I^{33,34}. Thus, its biological activity may mimic or be complementary to that of pan anti-MHC-I mAbs²⁹.

With recent technical and computational improvements, cryo-EM has become a valuable tool for determining the structures of protein complexes³⁵. However, obtaining high-resolution structures of asymmetric complexes of modest molecular weight (less than 200 kDa) remains challenging³⁶. Although some cryo-EM structures (using rigid and highly symmetric oligomeric scaffolds) have been determined at atomic resolution^{37,38}, dynamic flexible molecules (e.g. full-length antibodies) remain difficult^{37,39}. Here, we successfully determined the cryo-EM structures of complexes of B1.23.2 Fab and a B1.23.2 mAb in complex with the human HLA-B*44:05, at 3.31 Å and 3.02 Å resolution, respectively, as well as an X-ray crystal structure of B1.23.2 Fab complexed with HLA-B*44:05. These structures definitively describe the B1.23.2/HLA-B*44:05 interface and provide a structural paradigm for the informed application of B1.23.2 to reverse the

effects of immune inhibitory receptors such as KIR2DL and KIR3DL. Analysis of these structures in the context of previously studied KIR/HLA and LILR/HLA complexes suggested that B1.23.2 would induce activation of human NK cells leading to anti-tumor activity. We show that B1.23.2, engineered to eliminate potential complications due to Fc receptor interactions, stimulates proliferation and activation of human PBMC-derived NK cells in culture and can lead to control of tumor growth in NSG-IL15 mice. Such structure-guided treatment offers potential benefits of anti-MHC approaches for cancer immunotherapy.

RESULTS

Binding of B1.23.2 to HLA-A, -B and -C

Previous studies showed that B1.23.2 blocked the binding of recombinant KIR2DS1 and KIR2DL1 to HLA-C*04:01 transfectants³³. In addition, B1.23.2 inhibits the interaction of a KIR2DL1 reporter cell with HLA-C*02:02/04:01⁺ fibroblasts and partially blocks a KIR2DS1 reporter³⁴. We extended these experiments using an engineered, recombinant B1.23.2, which blocked the staining of human PBMC-derived CD14⁺ monocytes or of single HLA-B or -C transfectants by recombinant soluble KIR2DL2 and KIR2DL3, and by KIR3DL1²⁹. Using surface plasmon resonance (SPR), we show that recombinant B1.23.2 binds to HLA-B*44:05 with a K_D = 0.02 μ M (Fig. 1a), which is stronger than the range of affinities reported for KIR/HLA interactions (Supplementary Fig. 1a)^{6,40,41}. B1.23.2, originally reported to react with an HLA-A, -B positive cell line, independent of the β_2 m light chain at a site distinct from W6/32³¹, binds a broad panel of different HLA molecules, including all HLA-B and HLA-C tested³². We evaluated the specificity of binding of the recombinant B1.23.2 mAb to a standard panel of HLA-A, -B, and -C allelomorphs (Supplementary Fig. 1b). Using the pan anti-HLA mAb W6/32 as a reference⁴², we

observed that B1.23.2 binds all HLA-A, -B, and -C molecules tested with the exception of HLA-A*02:01, -A*02:03, -A*02:06, -A*68:01, -A*68:02, and -A*69:01. Consistent with these results, B1.23.2 stained cells individually transfected with HLA-B*44:05 and HLA-C*03:04, but failed to stain those expressing HLA-A*02:01, HLA-E*01:01, or HLA-G*01:01 (Supplementary Fig. 1c). Together, these results indicate that B1.23.2 blocks KIR2 and KIR3 binding to HLA, binds HLA with nanmolar affinity, and shows broad reactivity to HLA-A, -B, and -C allelomorphs.

Cryo-EM structure of anti-MHC-I mAb B1.23.2 in complex with HLA-B*44:05

To understand how B1.23.2 blocks the binding of KIRs to their MHC ligands, we determined cryo-EM structures of the complex of B1.23.2 with HLA-B*44:05 using both a full-length engineered Ab and the Fab derived from the murine hybridoma. Complexes of B1.23.2 mAb with bacterially expressed and refolded recombinant peptide/HLA-B*44:05/β₂m were produced, and cryo-EM images were collected as described in the Methods. Using cryoSPARC⁴³, we developed a protocol that improved map resolution for small molecular weight nonglobular complexes (Supplementary Fig. 2). Table 1 summarizes the data collection, statistics, and validation for the two cryo-EM structures of B1.23.2 mAb/HLA-B*44:05 and B1.23.2 Fab/HLA-B*44:05 complexes as well as for the Fc region images collected from the B1.23.2 mAb/HLA-B*44:05 complex. (Amino acid sequences are presented in Supplementary Table 1).

The cryo-EM structures determined from both the full length B1.23.2 mAb and Fab complexes with HLA-B*44:05 were very similar. The resolution of the mAb-containing complex was slightly better, and we discuss this structure first. Fig. 1b shows the 2D classification of particles of B1.23.2 mAb/B*44:05, revealing shapes clearly consistent with the expected Fab/HLA-B*44:05/β₂m complex (Fig. 1c). We noticed multiple distinct images among the 2D classes – some appear as Fab complexed with MHC-I; others look like Fc alone. We did not

observe individual particles representing full-length mAb, likely due to the flexibility of the hinge between Fab and Fc. The final refined map of the Fab/HLA images from the full-length mAb-containing sample (Fig. 1d) clearly showed all eight domains (V_H , C_{H1} , V_L , C_{κ} of the mAb and $\alpha 1$, $\alpha 2$, $\alpha 3$, $\beta 2m$ of HLA-B*44:05) and the bound peptide. The model (Fig. 1e) that was fit to the map was refined and validated (Table 1). The cryo-EM map was based on 359,876 particles and resulted in a map of resolution 3.02 Å, as shown in Fig. 1f,g.

Analysis of the contacts at the B1.23.2/HLA-B*44:05 interface reveals that the major focus of the antibody V_H and V_L is the HLA $\alpha 2_1$ helical segment. The Fab/HLA complex has a buried surface area (BSA) of 899 Å² consistent with many Ab/protein Ag interfaces (Fig. 2a). Neither V_H nor V_L of B1.23.2 interacts with $\beta 2m$. The details of the interactions are shown in Fig. 2b and Supplementary Table 2 and a contact map in Fig. 2c. The complementarity determining region (CDR) loops of V_H and V_L recognize the conserved residues on the $\alpha 2_1$ helix of HLA-B*44:05. Interestingly, the entire $\alpha 2_1$ helix of B*44:05 from Q141 to Q155 is buried tightly in a groove formed by V_H and V_L and constitutes the B1.23.2 epitope (Fig. 2a). K146 of HLA-B*44:05 is a major epitopic residue as it is bound by four residues (Y27, D87, Y86, and Y90) of V_L of B1.23.2 (Fig. 2b, right panel). Epitopic residues Q141, E148, A150 make multiple contacts with B1.23.2, and R145, R151, and A149 contact both V_H and V_L of B1.23.2 (Fig. 2c, Supplementary Table 2). Overall, Y28, W29, and Y95 of V_H , and Y27, Y44, and Y90 of V_L of B1.23.2 make the major contributions to the recognition of the $\alpha 2_1$ helix of B44:05, emphasizing the general role that tyrosine and tryptophan play in antibody recognition ⁴⁴.

Although we did not directly observe complete particles of full-length B1.23.2 with HLA-B*44:05 in a single stand-alone reconstruction, some additional density adjacent to the Fab fragment was observed. This density extends beyond the C_{H1} domain of the Fab in the full-length

B1.23.2 sample (Supplementary Fig. 3a, left panel), which likely represents part of the C_{H2} region of the Fc. We observed multiple types of particles in the micrographs from the full-length B1.23.2 sample – both Fab/HLA-B*44:05-like and Fc-like (Supplementary Fig. 3b). The Fc-like particles accounted for less than 10% of the total. Supplementary Fig. 3c illustrates some of the 2D classes of the Fc-like particles. The length of the Fc-like particles in the 3D reconstructed map measures about 100 Å, including a part of the C_{H1} domain (Supplementary Fig. 3d). This map was refined (using non-uniform refinement with 251,084 particles) to a resolution of 3.44 Å. Model fitting was challenging, largely due to disorder in the hinge region connecting C_{H1} to C_{H2} (Supplementary Fig. 3d). Using an hIgG1 Fc domain model generated by AlphaFold 3²⁷, we could fit part of the C_{H1} domain as well as C_{H2} and C_{H3} (Supplementary Fig. 3d, center). The two C_{H1} domains are twisted, and the hinge loops appear to form two “cross-over” disulfides^{45,46} at residues C222-C225 (Supplementary Fig. 3d, insert). Glycans linked through N293 of the C_{H2} domains were also identified. By overlaying the C_{H1} domains identified in the Fc maps with the extension seen on some Fab images, we constructed composite full-length models of B1.23.2 (Supplementary Fig. 3e) in which the angle between the two Fabs may vary from 90° to 100°. Light chain residues are seen to sterically compete with other density in the hinge region, suggestive of flexibility, mobility, and dynamics – precluding the detailed visualization of the whole B1.23.2 antibody.

Cryo-EM structure of anti-MHC-I Fab of B1.23.2 in complex with HLA-B*44:05

In parallel with the structure determination of the complex of the full B1.23.2 mAb/HLA-B*44:05 as presented above, we also collected cryo-EM data for a complex of the Fab of B1.23.2 bound to HLA-B*44:05 and solved the structure to a resolution of 3.31 Å (Supplementary Fig. 4). The models derived from the two (Fab/B44:05 vs. full mAb/B44:05) are essentially identical (see Discussion).

X-ray structure of B1.23.2 Fab/HLA-B*44:05 complex

We also determined the X-ray crystal structure of the complex of B1.23.2 Fab and HLA-B*44:05 (PDB ID: 8TQ6) (Supplementary Fig. 6a) to a resolution of 3.20 Å. Data collection and refinement statistics are given in Table 2. Electron density maps (2mFo-DFc, contoured at 1.5σ) for the CDR loops of H chain and L chain of B1.23.2 Fab interacting with $\alpha 2_1$ helix are shown in Supplementary Fig. 6b. Comparison of the X-ray crystal structure (8TQ6) with the two cryo-EM structures (PDB IDs: 9D73 and 9D74) shows very little difference in RMSD or BSA values, with RMSD values of approximately 1.5 Å for all atoms (Supplementary Fig. 6c). The BSA values at the antibody/antigen interfaces for X-ray crystal structure are slightly smaller than for the cryo-EM structures. Although the X-ray and cryo-EM-determined structures depend on fundamentally distinct methodologies and resolution is evaluated by different standards (see Discussion), the quality of the maps was very similar, and the identification of the interface residues of B1.23.2 with HLA-B*44:05 was in complete agreement.

Peptide variants at position 8 influence affinity of B1.23.2 for HLA-B*44:05

Analysis of the interface between B1.23.2 and HLA-B*44:05 revealed direct contacts between Y32 of CDRL1 of B1.23.2 and the carbonyl O at peptide position 8 (S) (Fig. 3a). B1.23.2 Y32 also forms an H-bond to HLA-B*44:05 W147, a highly conserved HLA residue critical to orienting the penultimate peptide residue in almost all known MHC-I structures. Light chain CDRL1 residue N30 also has a long distance contact to the peptide S8 side chain. To evaluate the possibility that peptide variants at position 8 might influence the binding affinity of B1.23.2 to HLA-B*44:05, we refolded HLA-B*44:05 with each of 19 peptides with position 8 substitutions and evaluated their binding to B1.23.2 (Fig. 3b). The different complexes bound B1.23.2 with a spectrum of K_D values ranging from ~8 nM (for the T substitution) to about 90 nM (for E) – 10-

fold weaker. Complexes prepared with acidic peptide amino acids at position 8 (E, D, and C) were weaker binders to B1.23.2, and T or substitutions with basic amino acids (K, R, and H) were slightly stronger (Fig. 3b). To understand the structural basis of these relatively small differences in affinity, we generated energy-minimized models of the structures with the substituted peptides (see Methods). Substitutions of the side chain at position 8 showed variation in the interaction with N30 of the B1.23.2 V_L CDRL1 (Supplementary Fig. 5a). Specifically, with T substitution, the position 8/N30 H-bond is slightly shorter, that with K is about the same, and R is drawn even closer to N30. The general surface charge difference around peptide residue 8 is evident in electrostatic surface calculations (Supplementary Fig. 5b).

Mutations of epitopic residues on $\alpha 2_1$ of A*02:01 -- experiment and computation

Knowing that the main epitopic residues of HLA-B*44:05 are those of the $\alpha 2_1$ helix, and that HLA-A*02:01 and closely related allelomorphs (-A*02:03, -A*02:06, -A*68:01, -A*68:02, and -A*69:01) failed to bind B1.23.2 (Supplementary Fig. 1b), we transplanted HLA-B*44:05 residues onto the HLA-A*02:01 $\alpha 2_1$ helix and tested binding to B1.23.2 (Fig. 3c). Four residues of HLA-A*02:01, T142, K144, H145, and H151 are of particular interest (Fig. 3c), so several single and multiple mutants were generated. The binding affinities of pMHC complexes containing these substitutions are shown in Fig. 3d. Single HLA-A*02:01 mutants T142I and H145R as well as the double T142I/H145R mutant did not show any binding. The triple mutations (T142I/H145R/H151R) and (T142I/K144Q/H145R) improved the binding affinities to $K_D = 9.0 \mu\text{M}$ and $K_D = 0.04 \mu\text{M}$, respectively. The quadruple mutant (T142I/K144Q/H145R/H151R) bound even better than the HLA-B*44:05 molecule ($K_D = 0.007 \mu\text{M}$). These results indicate that HLA-A*02:01 can gain B1.23.2 reactivity upon localized substitutions in the epitopic region of HLA-A*02:01 consistent with the structural data.

We also performed molecular dynamics simulations (see Methods) to evaluate the contributions of the $\alpha 2$ domain differences between HLA-B*44:05 and HLA-A*02:01 to B1.23.2 recognition. Starting with a model of the V_H V_L domains of B1.23.2 bound to a fragment of HLA-B*44:05, we analyzed individual substitutions (HLA-B*44:05 to -A*02:01) I142T, Q144K, R145H, and R151H as well as the quadruple mutant (Supplementary Fig. 8a,b). The backbone root-mean-square-deviation (RMSD) trajectories and corresponding probability distributions were calculated for the $\alpha 2_1$ helix and flanking residues of HLA-B*44:05 and the indicated mutants (Supplementary Fig. 8c). HLA-B*44:05 displayed a narrow RMSD distribution of $2.96 \pm 0.64 \text{ \AA}$ (Supplementary Fig. 8d) and limited fluctuation (RMSF) (Supplementary Fig. 8e), indicative of a relatively stable structure throughout the simulation. In contrast, the mutants, especially Q144K and the quadruple mutant, showed broader and larger RMSD distributions (Supplementary Fig. 8c,d) reflecting increased conformational instability. In addition, the residue-wide RMSF of the V_H and V_L residues reveal greater flexibility due to mutation of the HLA epitope as compared with the complex with HLA-B*44:05 (Supplementary Fig. 8f,g). Thus, the MD simulations are consistent with the experimental binding characteristics of HLA-A*02:01 substitution mutants (Fig. 3d).

Structural comparison reveals competition between anti-MHC-I mAb and inhibitory cell ligands

To gain further insight into the potential value of B1.23.2 to block HLA/KIR interactions, we examined the site of interaction of B1.23.2 in comparison with structurally determined footprints of KIR inhibitory receptors on MHC-I. Although several KIR/HLA structures have been determined, we selected two for detailed comparison. We superposed the HLA-B*44:05 heavy chain of the B1.23.2/HLA-B*44:05 complex onto the HLA-C*03:04 heavy chain of the

KIR2DL2/HLA-C*03:04 complex (PDB-ID: 1EFX)⁴¹ (Fig. 4a) and onto HLA-B*57:01 of the KIR3DL1/HLA-B*B57:01 (PDB-ID: 3VH8) complex (Fig. 4b)⁴⁰. Remarkably, the V_L domain of B1.23.2 completely overlaps with the D2 domain of either KIR2DL2 or KIR3DL1. The footprints of B1.23.2, KIR2DL2, and KIR3DL1 on the MHC-I surfaces are illustrated in Fig. 4c. The conserved KIR residues (S133/D135/E106-for KIR2D or S228/D230/E201-for KIR3D)^{40,41,47} of the D2 domain that interact with HLA R145, K146, and R151 are substituted by Y32/Y91/D92/Y95 of the L chain of B1.23.2 in the Ab complex (Fig. 4d). The contacts of B1.23.2, KIR2DL2 and KIR3DL1 overlap on five major residues: R145, K146, A149, A150 and R151 of the $\alpha 2_1$ helix (Fig. 4d, Supplementary Table 2). Importantly, the binding affinity of B1.23.2 ($K_D = 0.02 \mu\text{M}$) is much higher than that of KIRs (K_D from 9.5 to 17 μM) for HLA (Supplementary Fig. 1a). Since B1.23.2 sterically competes for the same conserved site on the HLA $\alpha 2_1$ helix that is bound by KIR2DL2 and KIR3DL1, it may result in blocking the inhibitory signal given by these receptors to the NK cell. These structural comparisons explain the observed competition of this mAb with KIR binding^{29,33,34}. Unlike other mAbs that block target/NK cell interactions by binding of the mAb directly to the NK cell receptor⁴⁸⁻⁵³, B1.23.2 blocks by binding to the inhibitory ligand (the HLA molecule) itself (Supplementary Fig. 7). Thus, a single antibody with great cross reactivity for most HLA molecules has the potential to reverse the KIR2DL or KIR3DL-mediated suppression of NK activity. This effect may be similar to that observed for pan anti-MHC-I mAbs, such as M1/42 in the mouse^{11,54}, or W6/32 and DX17 in the human²⁹ that block interactions of other inhibitory receptors on NK and myeloid cells. Therefore, we propose a simplified mechanism by which anti-HLA mAb may block the inhibitory receptors of NK cells, as shown in Fig. 4e. When B1.23.2 binds to HLA, the interactions between KIRs and HLA are impeded, which may

result in canceling the inhibitory signal, thus enhancing the activation signal to suppress tumor growth.

B1.23.2 blocks KIRs, unleashes NK cell activation, and suppresses tumor growth

The structural mapping of the B1.23.2 binding site suggested that this mAb, by functionally blocking KIR2DL or KIR3DL interactions, would lead to NK cell activation. For these experiments we used the LALAPG-engineered B1.23.2, which fails to interact with any Fc receptors to avoid additional complicating factors. As shown in Fig. 5a, coculture of human PBMC with B1.23.2 LALAPG leads to increased staining with Ki67 (26.7 to 70.9 %) (Fig. 5a), an indication of cell proliferation, increased mTOR and pS6 expression in NK cells (Fig. 5b,c), and enhanced levels of IFN γ (25.5 to 55.5 %) (Fig. 5d). In addition, CD14 $^{+}$ monocytes were activated to modestly increase their production of IL15R α (Fig. 5e). To evaluate the potential of B1.23.2 in anti-tumor immunity, NSG-IL15 mice were given the KLM-1 human pancreatic tumor, then engrafted with human CD3 $^{+}$ cells, and monitored for tumor growth (Fig. 5f). Compared with isotype control treated animals, those that received B1.23.2 LALAPG showed significant reduction of tumor volume out to 30 days. Phenotypic analysis of the tumor infiltrating lymphocytes (TILs) from these tumors showed increased levels of activating natural cytotoxicity receptors, NKp46 (Fig. 5g) and NKG2D (Fig. 5h). Thus, B1.23.2, apparently by blocking interactions of NK inhibitory receptors on NK cells, results in tumor control in a humanized mouse model.

DISCUSSION

Here we describe two cryo-EM structures and the X-ray structure of a highly cross-reactive anti-HLA mAb, B1.23.2, in complex with HLA-B*44:05. These provide a clear view of the contacts and explain how this Ab competes for KIR2 and KIR3 binding to HLA molecules. In

addition to defining the HLA epitope, our analysis confirms the small influence of the HLA-bound peptide (position 8) to B1.23.2 binding, and explains the lack of specificity for a limited number of HLA-A*02:01 related allelomorphs. Study of several HLA-A*02:01 site-directed variants that gain binding activity not only confirms the identification of the epitopic region but also may provide insight for expanding the reactivity of B1.23.2 by selective mutagenesis. It is important to emphasize that B1.23.2 exhibits broad anti-HLA-A, -B, and -C reactivity but is distinct from several TCR mimic (TCRm) antibodies that exhibit restricted peptide and MHC recognition. Similar to W6/32 and DX17, pan anti-HLA antibodies that inhibit LILR interactions²⁹, B1.23.2 has broad reactivity but for KIR2 and KIR3 binding sites.

Comparison of B1.23.2 mAb/HLA-B*44:05 and B1.23.2 Fab/HLA-B*44:05 structures

X-ray crystal structures of relatively few full-length IgG antibodies with natural hinge regions have been reported (PDB IDs: 1IGT, 1IGY, 1HZH, 5DK3, and 6GFE)⁵⁵⁻⁵⁹. Two other complete structures were obtained of molecules with hinge deletions (Ab DOB⁶⁰ and PDB ID: 1MCO⁶¹). Although cryo-EM offers to provide structural information of larger complexes than crystallography, few complete antibody complexes have been reported by this method. Most cryo-EM structures for antibodies appear as Fab despite efforts to use the full-length form of the antibody. Recently, cryo-EM structures of IgM Fc-pentamers (PDB ID: 6KXS, and 8BPE^{62,63}), and a full-length IgM pentamer (PDB ID: 8ADY⁶⁴) have been described. In negative stain images, IgG showed multiple forms of full-length antibodies with variation of the hinge angle between Fc and Fab and different elbow and rotation angles between Fabs⁵⁹. The challenge presented by full-length antibodies for cryo-EM structure determination is the heterogeneity of such molecules due to the flexibility of the hinge joining the Fab and Fc domains. We did not directly observe the full length mAb B1.23.2 in complex with B*44:05 within a single reconstruction, but we were able to

observe the Fab and Fc domains separately, from which we constructed a plausible full length model of the mAb-HLA complex (Supplementary Fig.4e). The full-length images were obtained with a recombinant B1.23.2 consisting of the native murine Fab region spliced to human Fc. Whether this unique construction contributed to our ability to visualize overlapping density from Fab and Fc images is not known.

Comparing the two cryo-EM structures of the B1.23.2 Ab/HLA-B*44:05 (9D73) and the B1.23.2 Fab/HLA-B*44:05 (9D74), we found that the cryo-EM map resolution for the B1.23.2 Ab/HLA-B*44:05 at the Fab-HLA interface is better (3.0Å) than that of B1.23.2 Fab/HLA-B*44:05 (3.3Å) (Supplementary Fig. 4e). This suggests that in some cases, using a full-length antibody for cryo-EM structure determination may prove more favorable than using the Fab alone. In general, using the Fab rather than the whole mAb for the crystallization of complexes is more successful.

In a comparison of cryo-EM and X-ray crystal structures, we noticed that the B-factors of the cryo-EM structure are larger than those of the crystal. This reflects the inherent flexibility and dynamic nature of biomolecules in the solution state, frozen in ice that may result in greater background noise, while X-ray crystallographic structures, due to the solid state of the crystal lattice, tend to have relatively lower B-factors. In addition, resolution in the crystal structure is estimated from the X-ray data (obtained in reciprocal space) that represent an overall value for the whole electron density map, and the B-factor describes the uncertainty or mobility around each atomic center. The map resolution evaluated by FSC in a cryo-EM structure is visualized in the density map (real space), but it represents a likely maximum resolution of the map, and the B-factor in the cryo-EM structure describes the density distribution around the atomic center. Unlike the Free-*R* value⁶⁵ that is used in validation of X-ray crystal structures, the Q-score⁶⁶ is generally

employed to validate the model fit to the map in a cryo-EM structure. We observed that the map resolution at the interface of the complex for a cryoEM structure is higher than that for the surface (Supplementary Fig. 4e). Binding forces (interactions between the antibody and MHC-I) may partially stabilize the flexible CDR loops at the interface.

Correlation and competition between TCR, inhibitory receptors, and anti-MHC-I mAb

One application of mAb B1.23.2 of therapeutic value is to exploit its potential for blocking inhibitory receptor/HLA interactions. Since the site of B1.23.2 overlaps extensively with the interface exploited by KIR2 and KIR3 receptors, it is effective in activating NK cell populations. In general, $\alpha\beta$ TCR, although as a group they describe a range of $\alpha 1$, $\alpha 2$, and peptide footprints⁹, by and large cover a region that overlaps, in part, with the footprint of B1.23.2. By contrast, B1.23.2 focuses on the $\alpha 2_1$ helix, while most TCR engage a centrally-located region including residues from $\alpha 1$, $\alpha 2$, and peptide (Supplementary Fig. 7a). For example, BSA between $\alpha\beta$ TCR and pMHC, for a TCR/peptide/HLA-B*44:05 complex (3KPR), is about 1340 Å², while the BSA of B1.23.2 with pMHC is 899 Å² (Fig. 4c). Unlike $\alpha\beta$ TCR, $\gamma\delta$ TCR reveal a wider variety of interaction sites on pMHC, in part reflecting their ability to bind non-classical MHC-I molecules such as CD1 or MR1⁶⁷. In Supplementary Fig. 7a we illustrate the contact residues on pMHC-I seen by TCR, KIR, and B1.23.2, respectively, and how they overlap. KIR binds many of the same MHC-I residues as do TCR and interacts with at least two peptide residues. B1.23.2 overlaps with KIR only on the $\alpha 2_1$ helix and one peptide residue at position 8. Five residues on the $\alpha 2_1$ helix would be expected to interact with some $\alpha\beta$ TCR^{9,68}, but not all $\gamma\delta$ TCR⁶⁷. It is noteworthy that B1.23.2 fails to bind the most common HLA allelomorph, HLA-A*02:01, and this characteristic may prove valuable as an adjunct to HLA-A*02:01-targetted CAR-T cell therapy by augmenting NK cell responses.

Supplementary Fig. 7b illustrates a mechanistic model for the competitive relations of the anti-MHC-I mAb and the inhibitory receptor of NK cell, as a mechanism distinct from the effects of other checkpoint inhibitors (anti-PD1 or anti-PDL1) (Supplementary Fig. 7c).

Despite exceptional progress in the treatment of a host of malignancies using antibodies directed against tumor-associated and neoantigens⁶⁹, the striking effects of antibodies that function as checkpoint inhibitors⁷⁰, and the rapid development of strategies to engineer bespoke reagents such as CAR-T cells⁷¹, there remains room for approaches that may harness NK and myeloid cell activation to augment cancer treatments⁷². Several groups have developed anti-inhibitory receptor mAb to block HLA/KIR or HLA/NKG2A interactions^{33,50,51,73}. We have previously shown that the pan anti-MHC-mAbs, M1/42 in the mouse, and W6/32 and DX17 in the human, that block engagement of tumor cells by the Ly49 or LILR inhibitory receptors on NK or myeloid cells, result in strong anti-tumor responses^{11,12,29}. Here we show that another widely reactive mAb, B1.23.2, binds almost all HLA-A, -B, and -C molecules at a site distinct from the W6/32, DX17 site, and which blocks KIR2 and KIR3 interactions with HLA, and has the potential to augment NK cell activity. Further studies of this and similar mAbs offer a novel avenue to complement current therapies. Here, from a structural viewpoint, we describe a highly cross-reactive anti-HLA class I mAb (B1.23.2) that can block inhibitory KIR/HLA interactions and has the potential to add to a multipronged approach to tumor treatment. It is unlikely that any single antibody can result in effective activation of innate immune cells by blocking inhibitory receptors throughout the full course of therapy, but different antibodies directed against different inhibitory ligands and checkpoint inhibitors may contribute to progress in the course of treatment. The particular value of antibodies like B1.23.2 is that while blocking KIR/HLA interactions, they would spare the

interaction of clonotypic TCR recognizing HLA-A*02:01-peptide complexes. Further studies of this and similar mAbs offer a novel avenue to complement current therapies.

METHODS

Recombinant proteins

The B1.23.2 hybridoma (mouse IgG2a)³¹ was a kind gift of Dr. Bernard Lafont. RNA was extracted from 10⁷ cells grown in DMEM (Lonza) supplemented with 10% fetal calf serum, glutamine, non-essential amino acids, HEPES, and 50 µg/ml gentamicin, using a total RNA extraction kit (New England Biolabs) following manufacturer's instructions. cDNA was prepared from 5 µg total RNA with the One-Taq RT PCR kit (New England Biolabs) following manufacturer's protocol. A panel of mouse immunoglobulin V-gene PCR primers⁷⁴ was used to amplify the expressed H and L chain V genes by RT-PCR followed by DNA sequencing. DNA encoding the H chain V sequence fused to the C_{H1} domain of human IgG1 was synthesized by Genscript (Genscript USA) and cloned by InFusion cloning (Takara) into a pcDNA3.1(+) vector encoding the human IL-10 signal sequence and the C_{H2} and C_{H3} domains of human IgG1. To prevent interaction with mouse and human Fc receptors three mutations, L234A, L235A, and P329G⁷⁵ were introduced in the Fc region of B1.23.2. Similarly, DNA encoding the L chain V sequence was fused to mouse C_K and cloned into pcDNA3.1(+) downstream of the human IL-10 signal sequence. H and L chain plasmids were transfected into exponentially growing HEK293S cells using ExpiFectamineTM and enhancers (GIBCO) following manufacturer's protocol. Seven days after transfection, secreted antibody was affinity purified on Protein A Sepharose (Cytiva) followed by size exclusion chromatography on Superdex 200 (Cytiva) in 25 mM TRIS pH 8, 150

mM NaCl. This recombinant full-length antibody is referred to as “mAb B1.23.2” throughout the paper.

To prepare Fab, 20 mg of the mouse antibody (purified from B1.23.2 hybridoma supernatant) was digested with immobilized papain (Thermo Scientific) for 4 hours at 37 °C in phosphate buffered saline (PBS) containing 20 mM cysteine and 2 mM EDTA. Following dialysis overnight against PBS, Fc fragments and undigested antibody were removed by Protein A Sepharose (Cytiva) chromatography and the Fab preparation was further purified by size exclusion chromatography on Superdex 200 (Cytiva).

Bacterial expression, refolding, and purification of the luminal domains of HLA-B*44:05 complexed with human β_2 m and the nonamer peptide, EEFGRAFSF representing residues 46-54 of the human HLA-DPA1*02:01, were performed as described previously⁷⁶. Similar expression, refolding and purification for each of 19 peptide variants at P8 of the peptide was accomplished.

Surface Plasmon Resonance (SPR)

SPR experiments were carried out in a BiaCore T200 (Cytiva, Uppsala, Sweden) at 25 °C in 10 mM TRIS pH 7.4, 150 mM NaCl, 3 mM EDTA, and 0.05% Surfactant P20. B1.23.2 whole antibody was covalently coupled to a CM5 chip to 600 RU via amine coupling chemistry with EDC/NHS. Using the single cycle kinetics method, serial 2-fold dilutions of MHC-I ranging from 500 nM to 31.2 nM were sequentially injected over the antibody surface at a flow rate of 20 μ L/min. Each injection was for 120 seconds followed by a 120 second dissociation phase before the next MHC-I concentration was injected. Regeneration was carried out at the end of the final cycle with a 15 second injection of 0.1M glycine/0.15M NaCl pH 2.3 at 30 μ L/min. Binding experiments were repeated three times. Sensorgrams were globally fit to a 1:1 binding model with

BiaCore T200 Evaluation Software 3.1 and plotted with Prism (GraphPad Software, San Diego, CA, USA).

Screening of reactivity of B1.23.2 for binding to a panel of HLA-A, -B, -C molecules.

Single antigen beads (SABs) are fluorescently color-coded and coated with 97 different HLA allotypes loaded with peptides derived from Epstein-Barr virus (EBV)-transfected cell lines. Biotinylated mAbs B1.23.2 and W6/32 were tetramerized using Streptavidin-phycoerythrin (PE; Agilent Technologies Inc.) at a final concentration of 0.5 mg/mL. The resulting B1.23.2 and W6/32 tetramers were each diluted at a staining ratio of 1:50 and mixed with 4 µL of LABScreen SAB suspension (OneLambda Inc., CA, USA) to a final volume of 24 µL in a 96-well plate. Samples were then incubated with either B1.23.2 or W6/32 tetramer for 1 hour at RT with shaking at 550 rpm, washed four times with wash buffer (OneLambda Inc., CA, USA) to remove excess tetramers, and resuspended in phosphate-buffered saline (PBS; pH 7.2). The mean fluorescence intensity (MFI) of SABs upon incubation with B1.23.2 or W6/32 was measured by the Luminex 100 Liquid Array Analyzer System. The experiment was conducted in duplicate. The MFI ratio was then calculated by dividing the average MFI of B1.23.2 by the average MFI of W6/32. The results were analyzed and plotted in GraphPad Prism v10.

Flow cytometry

For surface staining, HeLa cells (1×10^6) that express individually transfected HLA molecules, in staining buffer (PBS, 10% heat-inactivated FBS, and 0.05% sodium azide), were incubated with the following surface conjugate antibodies in 1:50 dilutions: anti-HLA-A2 (mAb BB7.2, BD Biosciences 568757), Anti-HLA-B (mAb YTH 76.3, BD Biosciences 567211), Anti-HLA-C (DT-9, BD Biosciences 566372), Anti-HLA-E (3D12, BD Biosciences 567418), Anti-HLA-G (87G, Biolegend 335912), B1.23.2 (ThermoFisher 17-5935-42) and DX17 (BD

Biosciences 560169) in the presence of Fc block (BD biosciences). Cells were washed with FACS staining buffer and acquired by LSRFortessa (BD Biosciences) flow cytometer with FACSDiva software and analyzed by FlowJo (tree star version 10) software.

hPBMC from healthy donors were suspended in complete RPMI-1640 medium. For surface staining, the cells were initially blocked using FCX Trustain (Biolegend) for 5 minutes, followed by staining with the surface conjugate for 20 minutes in FACS staining medium (PBS, 10% heat-inactivated FBS, and 0.05% sodium azide). Intracellular staining was done by fixing and permeabilizing the surface-stained cells with eBioscience™ Foxp3 / Transcription Factor Staining Buffer Set (ThermoFisher Cat # 00-5523-00) for 15 minutes and then staining with Ki-67 (BD Bioscience: Cat No 571538), p-mTOR (ThermoFisher Cat # 25-9718-42) and pS6 (ThermoFisher Cat # 48-9007-42) antibodies. To perform intracellular IFN γ staining, PBMC in complete RPMI medium were stimulated with a cocktail of cell stimulation and protein transport inhibitors (Thermo Fisher Cat # 00-4975-03) containing PMA, ionomycin, Brefeldin A, and monensin for 3-4 hours at 37°C. Cells were washed, fixed, permeabilized, and stained with anti-IFN γ antibody (BD Biosciences Cat # 554701) overnight at 4°C. Finally, the cells were washed and analyzed using BD LSR Fortessa X-20 cell analyzer and BD FACSDiva Software version 8.0. Data further analyzed by Flowjo™ V10 (Treestar).

Mice

NSG-IL-15 mice (NSG-IL15, stock no. 030890) were purchased from Jackson Laboratories and housed under specific pathogen-free conditions. All mice were sex and age matched and used between 10 and 13 weeks of age. All animal protocols used in this study were approved by the National Institute of Allergy and Infectious Diseases Animal Care and Use

Committee (Protocol # LISB 15E). We have complied with all relevant ethical regulations for animal use. Euthansia was performed by CO₂ asphyxiation.

hPBMC culture with B1.23.2LALAPG mAb

Human peripheral blood mononuclear cells (hPBMC) were obtained from unidentified normal human blood bank donors. Written informed consent according to the US Common Rule was obtained from the individuals. All ethical regulations relevant to human research participants were followed. These studies are exempt from further ethical review by Institutional Review Board and were performed according to guidelines of the National Institute of Allergy and Infectious Diseases. Cells were suspended in RPMI 1640 complete medium supplemented with 10% FBS, 2 mM L-glutamine, 1 mM sodium pyruvate, 1 mM HEPES, 0.1 mM nonessential amino acids, 50 µM 2-mercaptoethanol, and 100 U/ml penicillin and streptomycin. 10 mg of B1.23.2 LALAPG or hIgG1LALAPG was added to 0.5x10⁶ mononuclear cells in 500 µL medium in 48-well plates (Falcon) and incubated for 72 hours.

Humanized mouse tumor model

KLM1 cancer cells were grown in DMEM medium supplemented with 10% heat-inactivated FBS, L-glutamine (2mM), sodium pyruvate (1mM), HEPES (10mM), non-essential amino acids (0.1mM), 2-mercaptoethanol (50µM), and penicillin and streptomycin (100U/ml). Sex- and age-matched hIL15 transgenic mice were injected subcutaneously (right flank region) with 1.5 x 10⁵ KLM1 cells suspended in 100 µL of sterile PBS. After 12 days of tumor cell engraftment (12 mice of original 16 injected with tumor), 10 x 10⁶ CD3⁻ hPBMC, isolated from healthy individuals by negative selection on magnetic beads (Miltenyi Biotec), were retro-orbitally injected into the tumor-bearing mice. hIgG1LALAPG and B1.23.2LALAPG (100µg in 100µL PBS, six tumor-bearing mice per group) were administered retro-orbitally (i.v.) twice a week for

two weeks. Tumor size was measured in three dimensions regularly using digital calipers, and tumor volumes were calculated by multiplying length x width x depth. On day 30 post tumor implant, tumors were excised under sterile conditions, and TILs were prepared after mincing the tumor into very small pieces and further dissociated by Gentle MACS tissue dissociator. The dissociated tissue was passed through a 70mm strainer (BD Falcon), washed and then treated with ACK lysing buffer to lyse RBC. The single-cell suspension of TILs was washed with FACS staining buffer and purified by percoll density gradient centrifugation.

Cryo-EM sample preparation and data collection

Freshly purified anti-human antibodies (full length “mAb B1.23.2 LALAPG” or Fab “Fab B1.23.2”) were incubated in a 1:1 molar ratio with bacterially expressed and refolded soluble peptide/HLA-B*44:05/h β 2m complexes prepared as described previously⁷⁶. The complexes were purified by size exclusion chromatography (SEC) and used at a concentration of 0.7-1.4 mg/ml for sample preparation. Samples were applied onto holey-carbon cryo-EM grids (C-flatTM Holey Carbon Grid Gold 1.2 μ m/1.3 μ m space 300 mesh (Protochip, NC USA)), which had been glow discharged for 60 seconds, blotted for 3 seconds, and plunged into liquid ethane with a Vitrobot Mark4 (Thermo-Fisher) at 4 °C and 95% humidity. Cryo-EM data on the selected regions with ideal ice thickness were collected on a Titan Krios 300-keV microscope (NICE/NIH Cryo-EM consortium). Images were acquired automatically with SerialEM⁷⁷ on a BioQuantum-K3 detector (Gatan) in super-resolution mode at 130x nominal magnification (0.83 Å/unbinned pixels) and a defocus range from -0.7 to -2.0 μ m. An exposure time of 0.05s per frame was recorded, with a total exposure of about 54.2 electrons/Å². Three raw data sets were collected: mAb B1.23.2+HLA-B*44:05 with 7,154 movies, and Fab B1.23.2+HLA-B*44:05 with 3,077 movies.

Image processing, map resolution improvement, and model fitting

All image processing, 2D class, 3D reconstruction, and map refinements were performed using cryoSPARC v4.4.1^{43,78,79}. Following "Patch Motion Correction," "Patch CTF Estimation," and "Curate Exposures," outliers of defocus range, defective micrographs, and low-resolution estimation of the CTF fit (>6 Å) were discarded. The "Blob Picker" was initially used with a particle diameter of 128 Å for picking particles. The box size used for 2D classification and following was 256 pixels. The initial "Blob Picker" resulted in only a few 2D classes with suitable particles. Subsequently, we used these initial 2D classes as templates for "Template Picker" and, following standard protocols ("Ab-Initio Reconstruction" and "Non-uniform Refinement") with several iterations, obtained a map resolution of about 4.0 Å for these antibody complexes.

A protocol for map resolution improvement for small molecular weight complexes

We developed a protocol for map resolution improvement by using cryoSPARC⁴³ as shown in Supplementary Fig. 2. A key parameter, "LowPass Filter" (LPF), for picking potent particles from the micrographs in the "Template Picker" procedure can be optimized (the default value is 20). LPF implies "signal/noise frequency"^{78,79}. We used multiple "Template Picker" procedures with various LPF parameters (from 20 to 5) concurrently. Followed by the standard "extract particle" and "2D classification", we may select some better 2D classes as the "template particles" for the next round of the multiple Template Picker procedure. An additional 2D classification was necessary to merge all selected particles and remove duplicates. The 3D classification could also remove some 3D groups with low-resolution particles. This protocol improves the map resolution, although it costs more computing time. We used multiple "Template Picker" with LPF (a,b) = (20,20); (15,15); (10,10); (5,5), where (a,b) is applied to (template, micrograph) respectively. The input particle templates were from previously refined particles. For the example of the mAb B1.23.2 + HLA-B*44:05 complex, we used concurrent Template pickers, iterating 5 times, that

extracted 1,525,615 particles, selected 664,724 particles, and removed duplicates, leaving 516,068 particles for Ab-Initio construction. By eliminating poor conformations and optimizing the 3D classification, 359,876 particles were used for the final refined map. The map resolution was improved to 3.02 Å (see Table 1). The same protocol was applied to the B1.23.2 Fab+HLA-B*44:05 data sets, and the final map resolution was improved to 3.31 Å (see Table 1), respectively.

Crystallization, Data Collection, and Refinement

Crystallization conditions were identified by screening hanging drops at 18 °C. Crystals of Fab B1.23.2+HLA-B*44:05 were obtained under 16% PEG 3350, 0.04M Na citrate, 0.06M Bis-Tris pH 8.8. However, crystals of mAb B1.23.2+HLA-B*44:05 first appeared pin-like or needle-like and failed to provide usable diffraction data. We finally obtained relatively larger crystals by seeding with the reservoir well diluted with 20-30% water. Crystals were cryoprotected in mother liquor containing 10% ethylene glycol and flash frozen in liquid nitrogen. Diffraction data were collected (at wavelength 1.033 Å, in N₂ stream at ~ 100 K) at Southeast Regional Collaborative Access Team (SER-CAT) beamline 22ID at the Advanced Photon Source, Argonne National Laboratory and processed with XDS⁸⁰ to 3.2 Å resolution for Fab B1.23.2+HLA-B*44:05 (Table 2). The final data set for Fab B1.23.2+HLA-B*44:05 was merged from 3 data subsets with different omega angles for greater completeness and higher resolution. The structures were solved by molecular replacement with Phaser⁸¹ using H2-D^d from PDB 5WEU and HLA-B*44:05 from PDB 7TUC as search models. We used the DX17 Fab (PDB-ID: 8TQ5) model with CDR loops trimmed off as an initial Fab search model, then manually rebuilt the CDR loops according to electron density and amino acid sequence. These molecular replacement models were subjected to several rounds of refinement with Phenix⁸² interspersed with manual building in Coot⁸³. All Fab sequences were established by PCR sequencing.

$R_{\text{work}}/R_{\text{free}} (\%)$ values for final refined models of Fab B1.23.2+HLA-B*44:05 are 24.2/27.5. Data collection and refinement statistics are summarized in Table 2. Ramachandran statistics for the final model of Fab B1.23.2+HLA-B*44:05 are 92.9, 6.2, and 0.9 for % favored, allowed, and outliers, respectively. Graphics figures were generated with PyMOL⁸⁴ and ChimeraX⁸⁵.

Cryo-EM structure determination and refinement

We used the X-ray crystal structure model (PDB: 8TQ6) to dock and manually fit the cryo-EM maps of mAb B1.23.2 +HLA-B*44:05 and Fab B1.23.2+HLA-B*44:05, respectively. We used Real-Space Refinement in Phenix⁸⁶, which includes rigid-body refinement. The MHC-I rigid-body domains consist of $\alpha 1\alpha 2+\text{peptide}$, $\alpha 3$, and $\beta 2\text{m}$ domains, and Fab consists of four rigid-body domains (V_L , C_κ , V_H , C_{H1}). Simulated annealing (SA) at the initial step, local grid search, and ADP refinement were included. Secondary structure restraints were applied. The final refined model compared with the map densities has an overall CC (Correlation Coefficient) of 0.84/0.84/0.75 (mask/volume/peaks) for mAb B1.23.2+HLA-B*44:05, and 0.76/0.76/0.68 for Fab B1.23.2+HLA-B*44:05, respectively. We also calculated Q-score of individual residues⁶⁶ for validation. Cryo-EM Data processing, refinement statistics, and model validation are listed in Table 1.

Computational methodology for molecular dynamics (MD) simulation

To investigate the specific interactions and dynamic behavior of the $\alpha 2_1$ helix of HLA-B*44:05 in complex with the antibody B1.23.2, we employed a restricted model that includes a fragment of the $\alpha 2$ domain (residues 127-158), along with the variable heavy (V_H) and light (V_L) chains of the B1.23.2. (Supplementary Fig. 8). Classical MD simulations were performed using the cryo-EM structure of the anti-MHC-I monoclonal antibody B1.23.2 in complex with HLA-B*44:05 (PDB ID: 9D73). The initial coordinates were obtained from the PDB structure. Five

HLA-B*44:05 point mutants, I142T, Q144K, R145H, R151H, and a quadruple mutant were generated using the mutagenesis tool in PyMOL by substituting residues of HLA-B*44:05 with the corresponding residues from HLA-A*02:01. Parameterization of all systems was carried out using the CHARMM-GUI interface with the CHARMM36 force field ^{87,88}. Each system was solvated using the TIP3P water model, ensuring a minimum buffer of 10 Å between solute and the box edge ⁸⁹. The periodic boundary condition box dimensions were set to $75 \times 75 \times 75 \text{ \AA}^3$, and sodium and chloride ions were added to neutralize the systems and mimic physiological ionic strength (pH 7.4). Each system contained approximately 38,913 water atoms. Simulations were performed using the NAMD 3.0.1 simulation package ⁹⁰. Long-range electrostatics were treated using the Particle Mesh Ewald (PME) method, and a cutoff of 10 Å was applied for van der Waals interactions⁹¹. Temperature and pressure were maintained at 300K and 1atm, respectively, using the Langevin thermostat and barostat. Initial energy minimization was conducted for 250,000 steps using the conjugate gradient algorithm to eliminate steric clashes and achieve a low-energy conformation. After energy minimization, the solvent equilibration was performed for 1ns at 300K at NVT ensemble. At each integration step, the velocities were reassigned from a new Maxwell distribution and the temperature was incremented by 0.0001K. To gradually relax the system, harmonic restraints were applied to protein atoms and reduced stepwise (99, 25, 1.0, 0.1, and 0.001 kcal/mol·Å²) over 1.25 ns. The SHAKE algorithm was used to constrain all bonds involving hydrogen atoms. A time step of 2fs was used for integration the equations of motion. Finally, production simulations were carried out under the NPT ensemble for 100 ns for each system. All trajectory analyses and molecular visualizations were performed using Visual Molecular Dynamics (VMD 1.9.1) ⁹².

Statistics and reproducibility

All data and plots were analyzed for statistical significance as indicated in the figure legends. X-ray and cryo-EM statistics are indicated in Tables 1 and 2.

FIGURE LEGENDS

Fig. 1 | HLA-B*44:05 binding to B1.23.2 Ab, 2D classification of images, and overall structure. **a.** Binding of HLA-B*44:05 to B1.23.2 by SPR (see Methods). Sequential injection concentrations were: 31nM, 62nM, 125nM, 250nM, and 500nM. Data points in red (every 250th data point is shown), and curve fit (using all data points) in black. (Source data for these graphs is in Supplementary Data 2). **b.** 2D classification of cryo-EM images after several runs of particle picking. **c.** The best 2D class shows domains of Fab and MHC-I. **d.** Cryo-EM map of the complex. **e.** Refined model (PDB ID: 9D73) with the same colors indicating each domain and peptide. **f.** The protocol used in template picking and the number of resulting particles in each step. **g.** Map resolution as indicated by FSC (Fourier Shell Correlation) at 0.143 reveals 3.02 Å resolution (no mask = 3.5 Å).

Fig. 2 | B1.23.2 interacts with HLA-B*44:05 through H and L chain CDR loop contacts. **a.** The footprints of B*44:05 on the surface of B1.23.2 are indicated as green, and the footprints of B1.23.2 on the surface of B*44:05 are shown as orange (heavy chain) and pink (light chain). The total Buried Surface Area (BSA) is 899 Å². **b.** Details of the interaction of CDR loops of the light and the heavy chains. Both chains contact the α_{21} helix (see Supplementary Table 2). **c.** A diagrammatic presentation of the contacts. The multiple contacts (from CDR loops of H or L chains) are aligned against the residues of the α_{21} helix. Contact between HLA-B*44:05 S8 and L chain Y32 is not shown.

Fig. 3 | Peptide variants at position 8 and polymorphic residues of the α 2 domain influence the affinity of B1.23.2 for HLA-B*44:05 and HLA-A*02:01. **a.** Superposition of two cryo-EM structures (9D73 and 9D74) and the X-ray structure (8TQ6) reveals that Y32 of B1.23.2 L chain consistently contacts the carbonyl O of S8 of the peptide and recognizes W147 of HLA-B*44:05, forming a double hydrogen-bonded tripartite interaction. N30 of B1.23.2 L chain has a long-distance contact (3.6-4.3 Å) with the side chain of S8 of the peptide. **b.** The binding affinities (K_D (nM)) of B1.23.2 with 19 substitutions at S8 of the peptide of EEFGRAFSF to HLA-B*44:05. Value of the K_D for the complex containing the wild-type peptide is indicated. K_D values were determined as technical triplicates from single cycle kinetics analysis of SPR sensograms as described in Methods. Error bars indicate S.E.M. **c.** Sequence alignment on α 2₁ helix of HLA-B*44:05 and -A*02:01, colors highlight differences. **d.** The binding data of HLA-A*02:01, the indicated α 2₁ mutants, and HLA-B*44:05 to B1.23.2. Colored circles indicate data points (showing 1/250 of the data points) and black lines show the curve fits based on all data. **e.** The binding affinity, K_D (μM), associated kinetic on rate (k_a) and off rate (k_d) is shown for each parental and mutant. ND, not detectable. Binding of HLA molecules and mutants to B1.23.2 was determined by SPR (see Methods). Source data for these graphs is in Supplementary Data 2.

Fig. 4 | B1.23.2 mAb contacts on HLA overlap with those of KIR. **a.** Superposition of KIR2DL2+HLA-C*03:01 (PDB ID: 1EFX) on B1.23.2+HLA-B*44:05 (PDB ID: 9D73) indicates the clash of the D2 domain of KIR2DL2 over V_L and V_H domains of B1.23.2. **b.** Superposed KIR3DL1+HLA-B*57:01 (PDB ID: 3VH8) on B1.23.2+HLA-B*44:05 (PDB ID: 9D73) indicates the clash of the D2 domain of KIR3DL1 over V_L and V_H domains of B1.23.2. **c.** Footprints from B1.23.2 (orange), KIR2DL2 (cyan), and KIR3DL1 (blue purple) on the surface of MHC-I. The

BSA are 899\AA^2 , 752\AA^2 , and 919\AA^2 for B1.23.2, KIR2DL2, and KIR3DL1, respectively. **d.** Alignment of overlapping contact residues on the $\alpha 2_1$ helix of HLA from B1.23.2 and KIRs (see Contacts in Supplementary Table 2). Amino acid residues of B1.23.2 (H and L), KIR2DL2, and KIR3DL1 that interact with the indicated HLA-B or -C residues are tabulated, revealing that the several HLA ligands compete for interaction with conserved HLA residues R145, K146, A149, A150 and R151. **e.** A mechanistic model illustrating how anti-MHC mAb (B1.23.2) may compete with KIRs. When B1.23.2 binds to HLA-B*44:05, the interactions between KIRs and HLA are blocked, which may cancel the inhibitory signal, thus allowing the activation signal to dominate.

Fig. 5 | B1.23.2 treatment stimulates NK cell proliferation and augments anti-tumor immunity. **a.** Human PBMC cultured with control or B1.23.2 LALAPG mAb for 72 hr were analyzed for Ki-67 on CD16+CD56dim NK cells. **b, c.** p-mTOR or pS6 staining of CD16+CD56dim NK cells is shown, indicating MFI values. **d.** Intracellular IFNg staining on CD16+CD56dim NK cells after 72 hr stimulation. **e.** IL-15Ra on CD14+ monocytes after 72 hr stimulation (% positive indicated). **f.** B1.23.2 LALAPG treatment controls human tumor (KLM-1) growth in NSG-IL15 mice. Treatment scheme illustrated (above) and day 30 tumor volume sizes are shown (upper row shows control hIgG1 LALAPG, lower row is B1.23.2 LALAPG (n=6-8)). MAb treatment started at Day 16. **g.** NKp46 and **h.** NKG2D expression on CD16+ TIL harvested on day 30. (Statistics reflect nonparametric, Mann-Whitney t-test, using Graphpad Prism, n=6 for each group). Gating strategies are provided in “Supplemental Material -Gating Strategies for Fig. 5.”

Table 1. Cryo-EM data collection, refinement and validation statistics

	B1.23.2Ab+HLA-B*44:05 (EMDB-46601) (PDB 9D73)	B1.23.2Fab+HLA-B*44:05 (EMDB-46602) (PDB 9D74)	B1.23.2Ab-Fc (EMDB-70276) (PDB 9OA9)
Data collection and processing			
Magnification	130,000	130,000	130,000
Voltage (kV)	300	300	300
Electron exposure (e ⁻ /Å ²)	54.2	54.2	54.2
Defocus range (μm)	-0.7 to -2.0	-0.7 to -2.0	-0.7 to -2.0
Pixel size (Å)	0.83 (binned)	0.83 (binned)	0.83 (binned)
Symmetry imposed	C1	C1	C1
Initial particle images (no.)	1,525,615	1,447,993	1,447,993
Final particle images (no.)	359,876	406,922	251,084
Map resolution (Å)	3.02	3.31	3.44
FSC threshold	0.143	0.143	0.143
Map resolution range (Å)	3.02-3.50	3.31-3.90	3.40-3.70
Refinement			
Initial model used (PDB code)	8TQ6	8TQ6	AlphaFold3
Model resolution (Å)	3.02	3.31	3.44
FSC threshold	0.143	0.143	0.143
Model resolution range (Å)	3.02-3.50	3.31-3.90	3.40-3.70
Map sharpening B factor (Å ²)	0	0	0
Model composition			
Non-hydrogen atoms	6,311	6,017	3,676
Protein residues	807	798	550
Ligands	0	0	12
B factors (Å ²)			
Protein	128.8	172.4	101.2
Ligand			
R.m.s. deviations			
Bond lengths (Å)	0.003	0.004	0.008
Bond angles (°)	0.618	0.682	1.302
Validation			
MolProbity score	2.50	2.71	1.64
Clashscore	11.65	16.56	51.75
Poor rotamers (%)	5.14	6.26	19.87
Ramachandran plot			
Favored (%)	94.48	94.40	68.90
Allowed (%)	5.52	5.60	28.19
Disallowed (%)	0.00	0.00	2.90

Table 2. X-ray crystallography Data collection and refinement statistics

B1.23.2Fab+HLA-B*44:05 (PDB-ID: 8TQ6)	
Data collection	
Space group	P2 ₁ 2 ₁ 2 ₁
Cell dimensions	
a, b, c (Å)	89.50, 92.84, 229.81
α, β, γ (°)	90.0, 90.0, 90.0
Resolution (Å)	49.30-3.20 (3.31-3.20)
R_{sym} or R_{merge}	0.329 (1.346)
$I/\sigma(I)$	5.6 (1.5)
Completeness (%)	95.7 (94.2)
Redundancy	4.6 (4.3)
CC _{1/2}	0.938 (0.435)
Refinement	
Resolution (Å)	49.30-3.20 (3.31-3.20)
No. reflections	31,179 (3,011)
$R_{\text{work}} / R_{\text{free}}$	24.2/27.5 (29.9/32.2)
No. atoms	
Protein	12,516
Ligand/ion	0
Water	0
B -factors (Å ²)	
Wilson Plot	45.1
Protein	47.7
Ligand/ion	0
Water	0
R.m.s. deviations	
Bond lengths (Å)	0.003
Bond angles (°)	0.72
Ramachandran	
favored (%)	92.9
allowed (%)	6.2
Outliers (%)	0.9

DATA AVAILABILITY

The cryo-EM maps were deposited in the Electron Microscopy Data Bank under the accession IDs EMD-46601 (3.02 Å), EMD-46602 (3.31 Å) and EMD-70276 (3.44 Å), and the atomic coordinates were deposited in the PDB under the accession ID 9D73, 9D74, and 9OA9.

X-ray crystal structure data and atomic coordinates were deposited in PDB under the accession ID 8TQ6. All source data for graphs, plots, and structures may be obtained from authors. Numerical source data for plots is found in Supplementary Data 1 (for Supplementary Fig. 1b) and Supplementary Data 2 (for Fig. 1a and Fig. 3d).

ACKNOWLEDGEMENTS

This work was supported by the Division of Intramural Research of the NIAID, NIH. X-ray data were collected at Southeast Regional Collaborative Access Team (SER-CAT) 22-ID (or 22-BM) beamline at the Advanced Photon Source, Argonne National Laboratory. SER-CAT is supported by its member institutions (www.ser-cat.org/members.html) and equipment grants (S10_RR25528 and S10_RR028976) from the National Institutes of Health. Use of the Advanced Photon Source was supported by the U. S. Department of Energy, Office of Science, Office of Basic Energy Sciences, under Contract No. W-31-109-Eng-38. The Electron Microscopy Resource is supported by the National Cancer Institute and NIH Intramural Research Program Cryo-EM Consortium (NICE). Access to the Luminex instrument was provided by Dr. Dimitri Monos (CHOP) and the CHOP Immunogenetics Laboratory.

AUTHOR CONTRIBUTIONS

JJ, KN, AKP, EMS and DHM conceived the study. JJ, KN, HL, JA, ZCL, AJM, and RKH collected cryo-EM data. JJ analyzed cryo-EM data and solved structures. JJ and KN collected and analyzed X-ray data. KN, LFB, and RRT purified protein and performed binding studies. SS and MM-S performed molecular dynamics studies and YS and NS analyzed antibody specificity. SC and AKP studied cell activation and tumorigenesis. JJ, KN, EMS, and DHM wrote and revised the paper.

COMPETING INTERESTS

The authors declare no competing interests.

REFERENCES

1. Margulies, D.H., Natarajan, K., Rossjohn, J. & McCluskey, J. The Major Histocompatibility Complex (MHC). in *Paul's Fundamental Immunology* (eds. Flajnik, M.F., Singh, N.J. & Holland, S.M.) 571–621 (Wolters Kluwer, 2023).
2. Blum, J.S., Wearsch, P.A. & Cresswell, P. Pathways of antigen processing. *Annu Rev Immunol* **31**, 443–73 (2013).
3. Bottino, C., Picant, V., Vivier, E. & Castriconi, R. Natural killer cells and engagers: Powerful weapons against cancer. *Immunol Rev* **328**, 412–421 (2024).
4. Brown, D., Trowsdale, J. & Allen, R. The LILR family: modulators of innate and adaptive immune pathways in health and disease. *Tissue Antigens* **64**, 215–25 (2004).
5. Malnati, M.S. et al. Peptide specificity in the recognition of MHC class I by natural killer cell clones. *Science* **267**, 1016–8 (1995).
6. Sim, M.J.W. et al. Innate receptors with high specificity for HLA class I-peptide complexes. *Sci Immunol* **8**, eadh1781 (2023).
7. Chapman, T.L., Heikeman, A.P. & Bjorkman, P.J. The inhibitory receptor LIR-1 uses a common binding interaction to recognize class I MHC molecules and the viral homolog UL18. *Immunity* **11**, 603–13 (1999).
8. Shiroishi, M. et al. Structural basis for recognition of the nonclassical MHC molecule HLA-G by the leukocyte Ig-like receptor B2 (LILRB2/LIR2/ILT4/CD85d). *Proc Natl Acad Sci U S A* **103**, 16412–7 (2006).
9. Marrack, P., Scott-Browne, J.P., Dai, S., Gapin, L. & Kappler, J.W. Evolutionarily conserved amino acids that control TCR-MHC interaction. *Annu Rev Immunol* **26**, 171–203 (2008).
10. Rossjohn, J. et al. T cell antigen receptor recognition of antigen-presenting molecules. *Annu Rev Immunol* **33**, 169–200 (2015).
11. Panda, A.K. et al. Cutting Edge: Inhibition of the Interaction of NK Inhibitory Receptors with MHC Class I Augments Antiviral and Antitumor Immunity. *J Immunol* **205**, 567–572 (2020).
12. Kohrt, H.E. et al. Anti-KIR antibody enhancement of anti-lymphoma activity of natural killer cells as monotherapy and in combination with anti-CD20 antibodies. *Blood* **123**, 678–86 (2014).
13. Panda, A.K. et al. Antibody-Mediated Inhibition of HLA/LILR Interactions Breaks Innate Immune Tolerance and Induces Antitumor Immunity. *Cancer Immunol Res* **13**, 1938–1955 (2025).
14. Vivier, E. et al. Innate or adaptive immunity? The example of natural killer cells. *Science* **331**, 44–9 (2011).
15. Paul, S. & Lal, G. The Molecular Mechanism of Natural Killer Cells Function and Its Importance in Cancer Immunotherapy. *Front Immunol* **8**, 1124 (2017).
16. Abel, A.M., Yang, C., Thakar, M.S. & Malarkannan, S. Natural Killer Cells: Development, Maturation, and Clinical Utilization. *Front Immunol* **9**, 1869 (2018).

17. Boyington, J.C. & Sun, P.D. A structural perspective on MHC class I recognition by killer cell immunoglobulin-like receptors. *Mol Immunol* **38**, 1007–21 (2002).
18. Natarajan, K., Dimasi, N., Wang, J., Mariuzza, R. & Margulies, D. Structure and function of natural killer cell receptors: Multiple molecular solutions to self, nonself discrimination. *Annual Review of Immunology* **20**, 853–885 (2002).
19. Kärre, K. Karolinska Institute (1981).
20. Karlhofer, F.M., Ribaudo, R.K. & Yokoyama, W.M. MHC class I alloantigen specificity of Ly-49+ IL-2-activated natural killer cells. *Nature* **358**, 66–70 (1992).
21. Tormo, J., Natarajan, K., Margulies, D. & Mariuzza, R. Crystal structure of a lectin-like natural killer cell receptor bound to its MHC class I ligand. *Nature* **402**, 623–631 (1999).
22. Li, Y. & Mariuzza, R.A. Structural basis for recognition of cellular and viral ligands by NK cell receptors. *Front Immunol* **5**, 123 (2014).
23. Myers, J.A. & Miller, J.S. Exploring the NK cell platform for cancer immunotherapy. *Nat Rev Clin Oncol* **18**, 85–100 (2021).
24. Maiorino, L., Dassler-Plenker, J., Sun, L. & Egeblad, M. Innate Immunity and Cancer Pathophysiology. *Annu Rev Pathol* **17**, 425–457 (2022).
25. Kyrysyuk, O. & Wucherpfennig, K.W. Designing Cancer Immunotherapies That Engage T Cells and NK Cells. *Annu Rev Immunol* **41**, 17–38 (2023).
26. Fenis, A., Demaria, O., Gauthier, L., Vivier, E. & Narni-Mancinelli, E. New immune cell engagers for cancer immunotherapy. *Nat Rev Immunol* **24**, 471–486 (2024).
27. Abramson, J. et al. Accurate structure prediction of biomolecular interactions with AlphaFold 3. *Nature* **630**, 493–500 (2024).
28. Lee, H.T. et al. Molecular mechanism of PD-1/PD-L1 blockade via anti-PD-L1 antibodies atezolizumab and durvalumab. *Sci Rep* **7**, 5532 (2017).
29. Panda, A.K. et al. Antibody Mediated Inhibition of HLA/LILR Interactions Breaks Innate Immune Tolerance and Induces Antitumor Immunity. *Cancer Immunol Res* (2025).
30. Pymm, P. et al. The Structural Basis for Recognition of Human Leukocyte Antigen Class I Molecules by the Pan-HLA Antibody W6/32. *J Immunol* **213**, 876–885 (2024).
31. Rebai, N. & Malissen, B. Structural and genetic analyses of HLA class I molecules using monoclonal xenoantibodies. *Tissue Antigens* **22**, 107–17 (1983).
32. Apps, R. et al. Human leucocyte antigen (HLA) expression of primary trophoblast cells and placental cell lines, determined using single antigen beads to characterize allotype specificities of anti-HLA antibodies. *Immunology* **127**, 26–39 (2009).
33. Stewart, C.A. et al. Recognition of peptide-MHC class I complexes by activating killer immunoglobulin-like receptors. *Proc Natl Acad Sci U S A* **102**, 13224–9 (2005).
34. van der Ploeg, K. et al. Modulation of Human Leukocyte Antigen-C by Human Cytomegalovirus Stimulates KIR2DS1 Recognition by Natural Killer Cells. *Front Immunol* **8**, 298 (2017).
35. Henderson, R. & Hasnain, S.;Cryo-EM: electron cryomicroscopy, cryo electron microscopy or something else? *IUCrJ* **10**, 519–520 (2023).
36. Wu, M. & Lander, G.C. How low can we go? Structure determination of small biological complexes using single-particle cryo-EM. *Curr Opin Struct Biol* **64**, 9–16 (2020).
37. Yip, K.M., Fischer, N., Paknia, E., Chari, A. & Stark, H. Atomic-resolution protein structure determination by cryo-EM. *Nature* **587**, 157–161 (2020).
38. Han, Y. et al. High-yield monolayer graphene grids for near-atomic resolution cryoelectron microscopy. *Proc Natl Acad Sci U S A* **117**, 1009–1014 (2020).

39. Wright, K.M. et al. Hydrophobic interactions dominate the recognition of a KRAS G12V neoantigen. *Nat Commun* **14**, 5063 (2023).

40. Vivian, J.P. et al. Killer cell immunoglobulin-like receptor 3DL1-mediated recognition of human leukocyte antigen B. *Nature* **479**, 401–5 (2011).

41. Boyington, J.C., Motyka, S.A., Schuck, P., Brooks, A.G. & Sun, P.D. Crystal structure of an NK cell immunoglobulin-like receptor in complex with its class I MHC ligand. *Nature* **405**, 537–43 (2000).

42. Hilton, H.G. & Parham, P. Missing or altered self: human NK cell receptors that recognize HLA-C. *Immunogenetics* **69**, 567–579 (2017).

43. Punjani, A., Rubinstein, J.L., Fleet, D.J. & Brubaker, M.A. cryoSPARC: algorithms for rapid unsupervised cryo-EM structure determination. *Nat Methods* **14**, 290–296 (2017).

44. Jiang, J. et al. SARS-CoV-2 antibodies recognize 23 distinct epitopic sites on the receptor binding domain. *Commun Biol* **6**, 953 (2023).

45. Orr, C.M. et al. Hinge disulfides in human IgG2 CD40 antibodies modulate receptor signaling by regulation of conformation and flexibility. *Sci Immunol* **7**, eabm3723 (2022).

46. Elliott, I.G. et al. Structure-guided disulfide engineering restricts antibody conformation to elicit TNFR agonism. *Nat Commun* **16**, 3495 (2025).

47. Joyce, M.G. & Sun, P.D. The structural basis of ligand recognition by natural killer cell receptors. *J Biomed Biotechnol* **2011**, 203628 (2011).

48. Lorig-Roach, N., Harpell, N.M. & DuBois, R.M. Structural basis for the activity and specificity of the immune checkpoint inhibitor lirilumab. *Sci Rep* **14**, 742 (2024).

49. Tian, J. et al. ILT2 and ILT4 Drive Myeloid Suppression via Both Overlapping and Distinct Mechanisms. *Cancer Immunol Res* **12**, 592–613 (2024).

50. Andre, P. et al. Anti-NKG2A mAb Is a Checkpoint Inhibitor that Promotes Anti-tumor Immunity by Unleashing Both T and NK Cells. *Cell* **175**, 1731–1743 e13 (2018).

51. van Montfoort, N. et al. NKG2A Blockade Potentiates CD8 T Cell Immunity Induced by Cancer Vaccines. *Cell* **175**, 1744–1755 e15 (2018).

52. Mandel, I. et al. BND-22, a first-in-class humanized ILT2-blocking antibody, promotes antitumor immunity and tumor regression. *J Immunother Cancer* **10** (2022).

53. Villa-Alvarez, M. et al. Ig-Like Transcript 2 (ILT2) Blockade and Lenalidomide Restore NK Cell Function in Chronic Lymphocytic Leukemia. *Front Immunol* **9**, 2917 (2018).

54. He, K. et al. Homeostatic self-MHC-I recognition regulates anti-metastatic function of mature lung natural killer cells. *Biochem Biophys Res Commun* **738**, 150906 (2024).

55. Harris, L.J. et al. The three-dimensional structure of an intact monoclonal antibody for canine lymphoma. *Nature* **360**, 369–72 (1992).

56. Harris, L.J., Larson, S.B., Hasel, K.W. & McPherson, A. Refined structure of an intact IgG2a monoclonal antibody. *Biochemistry* **36**, 1581–97 (1997).

57. Saphire, E.O., Parren, P.W., Barbas, C.F., 3rd, Burton, D.R. & Wilson, I.A. Crystallization and preliminary structure determination of an intact human immunoglobulin, b12: an antibody that broadly neutralizes primary isolates of HIV-1. *Acta Crystallogr D Biol Crystallogr* **57**, 168–71 (2001).

58. Scapin, G. et al. Structure of full-length human anti-PD1 therapeutic IgG4 antibody pembrolizumab. *Nat Struct Mol Biol* **22**, 953–8 (2015).

59. Blech, M. et al. Structure of a Therapeutic Full-Length Anti-NPRA IgG4 Antibody: Dissecting Conformational Diversity. *Biophys J* **116**, 1637–1649 (2019).

60. Silverton, E.W., Navia, M.A. & Davies, D.R. Three-dimensional structure of an intact human immunoglobulin. *Proc Natl Acad Sci U S A* **74**, 5140–4 (1977).

61. Guddat, L.W., Herron, J.N. & Edmundson, A.B. Three-dimensional structure of a human immunoglobulin with a hinge deletion. *Proc Natl Acad Sci U S A* **90**, 4271–5 (1993).

62. Li, Y. et al. Structural insights into immunoglobulin M. *Science* **367**, 1014–1017 (2020).

63. Chen, Q., Menon, R.P., Masino, L., Tolar, P. & Rosenthal, P.B. Structural basis for Fc receptor recognition of immunoglobulin M. *Nat Struct Mol Biol* **30**, 1033–1039 (2023).

64. Chen, Q., Menon, R., Calder, L.J., Tolar, P. & Rosenthal, P.B. Cryomicroscopy reveals the structural basis for a flexible hinge motion in the immunoglobulin M pentamer. *Nat Commun* **13**, 6314 (2022).

65. Brunger, A.T. Free R value: a novel statistical quantity for assessing the accuracy of crystal structures. *Nature* **355**, 472–5 (1992).

66. Pintilie, G. et al. Measurement of atom resolvability in cryo-EM maps with Q-scores. *Nat Methods* **17**, 328–334 (2020).

67. Sok, C.L., Rossjohn, J. & Gully, B.S. The Evolving Portrait of gammadelta TCR Recognition Determinants. *J Immunol* **213**, 543–552 (2024).

68. Roomp, K. & Domingues, F.S. Predicting interactions between T cell receptors and MHC-peptide complexes. *Mol Immunol* **48**, 553–62 (2011).

69. Xie, N. et al. Neoantigens: promising targets for cancer therapy. *Signal Transduct Target Ther* **8**, 9 (2023).

70. Sharma, P. et al. Immune checkpoint therapy-current perspectives and future directions. *Cell* **186**, 1652–1669 (2023).

71. Patel, K.K., Tariveranmoshabad, M., Kadu, S., Shobaki, N. & June, C. From concept to cure: The evolution of CAR-T cell therapy. *Mol Ther* (2025).

72. Vivier, E. et al. Natural killer cell therapies. *Nature* **626**, 727–736 (2024).

73. Carlsten, M. et al. Checkpoint Inhibition of KIR2D with the Monoclonal Antibody IPH2101 Induces Contraction and Hyporesponsiveness of NK Cells in Patients with Myeloma. *Clin Cancer Res* **22**, 5211–5222 (2016).

74. Wang, Z. et al. Universal PCR amplification of mouse immunoglobulin gene variable regions: the design of degenerate primers and an assessment of the effect of DNA polymerase 3' to 5' exonuclease activity. *J Immunol Methods* **233**, 167–77 (2000).

75. Lo, M. et al. Effector-attenuating Substitutions That Maintain Antibody Stability and Reduce Toxicity in Mice. *J Biol Chem* **292**, 3900–3908 (2017).

76. Jiang, J. et al. Structural mechanism of tapasin-mediated MHC-I peptide loading in antigen presentation. *Nat Commun* **13**, 5470 (2022).

77. Mastronarde, D.N. Automated electron microscope tomography using robust prediction of specimen movements. *J Struct Biol* **152**, 36–51 (2005).

78. Punjani, A., Zhang, H. & Fleet, D.J. Non-uniform refinement: adaptive regularization improves single-particle cryo-EM reconstruction. *Nat Methods* **17**, 1214–1221 (2020).

79. Punjani, A. & Fleet, D.J. 3DFlex: determining structure and motion of flexible proteins from cryo-EM. *Nat Methods* **20**, 860–870 (2023).

80. Kabsch, W. Xds. *Acta Crystallogr D Biol Crystallogr* **66**, 125–32 (2010).

81. McCoy, A.J. et al. Phaser crystallographic software. *J Appl Crystallogr* **40**, 658–674 (2007).

82. Adams, P.D. et al. PHENIX: a comprehensive Python-based system for macromolecular structure solution. *Acta Crystallogr D Biol Crystallogr* **66**, 213–21 (2010).

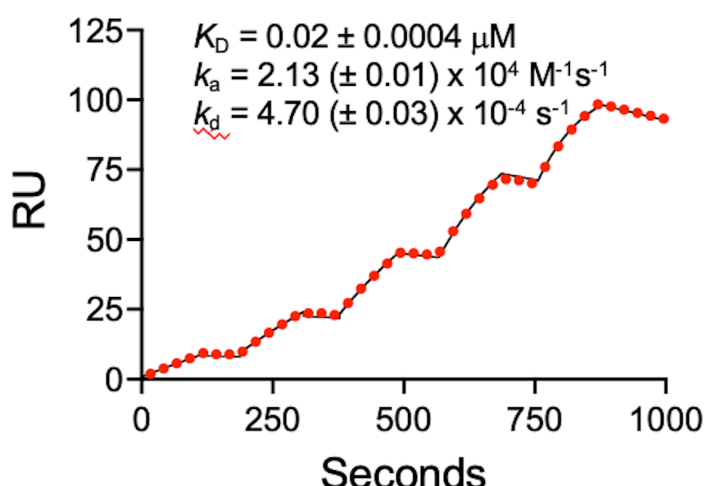
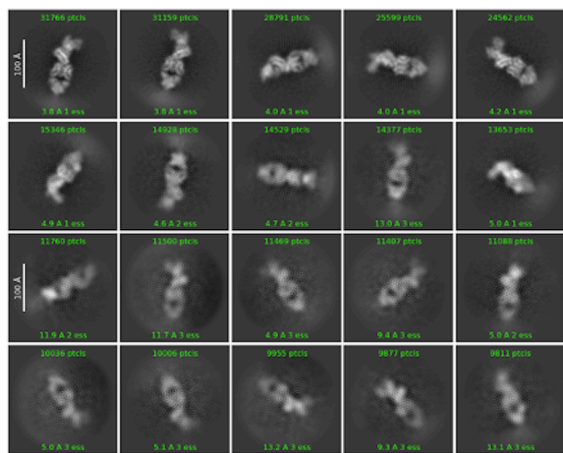
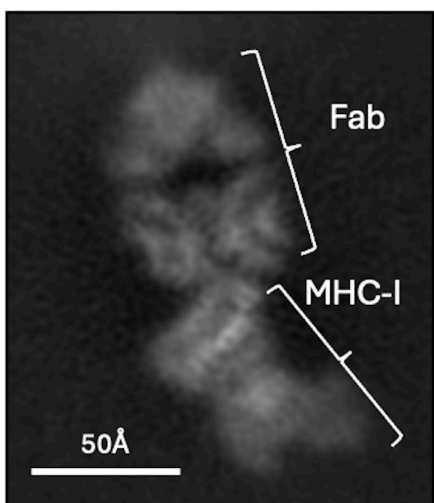
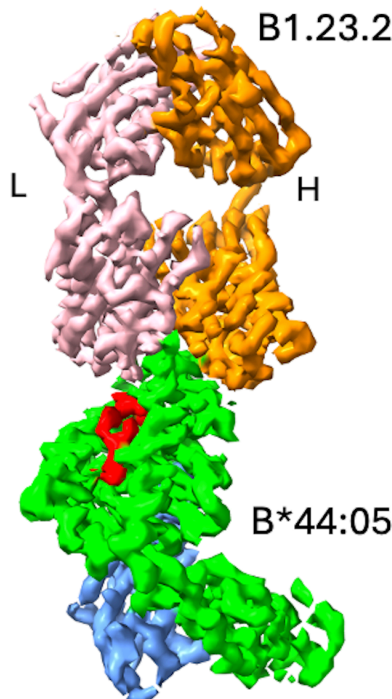
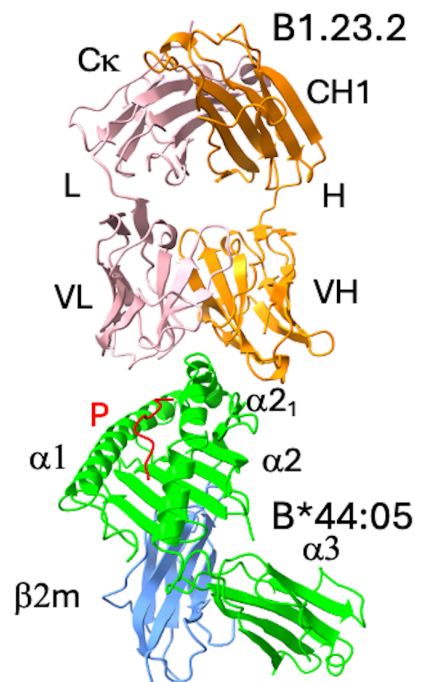
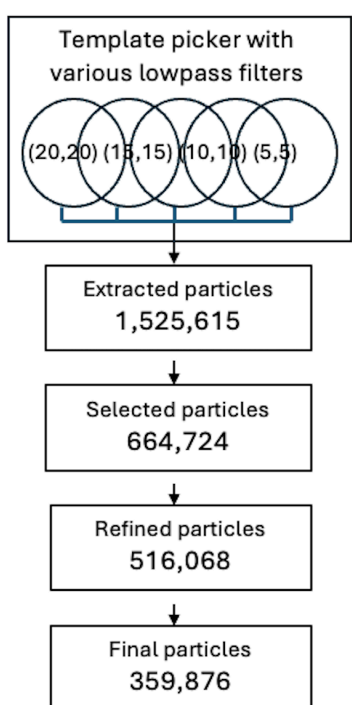
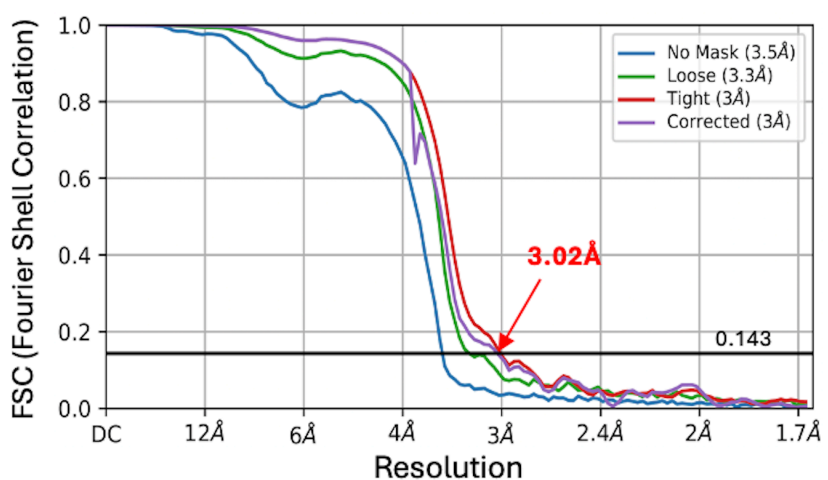
83. Emsley, P., Lohkamp, B., Scott, W.G. & Cowtan, K. Features and development of Coot. *Acta Crystallogr D Biol Crystallog* **66**, 486–501 (2010).
84. PyMOL. The PyMOL Molecular Graphics System, Version 3.0 Schrödinger, LLC.
85. Meng, E.C. et al. UCSF ChimeraX: Tools for structure building and analysis. *Protein Sci* **32**, e4792 (2023).
86. Liebschner, D. et al. Macromolecular structure determination using X-rays, neutrons and electrons: recent developments in Phenix. *Acta Crystallogr D Struct Biol* **75**, 861–877 (2019).
87. Huang, J. & MacKerell, A.D., Jr. CHARMM36 all-atom additive protein force field: validation based on comparison to NMR data. *J Comput Chem* **34**, 2135–45 (2013).
88. Jo, S., Kim, T., Iyer, V.G. & Im, W. CHARMM-GUI: a web-based graphical user interface for CHARMM. *J Comput Chem* **29**, 1859–65 (2008).
89. Jorgensen, W.L., Chandrasekhar, J., Buckner, J.K. & Madura, J.D. Computer simulations of organic reactions in solution. *Ann N Y Acad Sci* **482**, 198–209 (1986).
90. Phillips, J.C. et al. Scalable molecular dynamics with NAMD. *J Comput Chem* **26**, 1781–802 (2005).
91. Darden, T., York, D. & Pedersen, L. Particle Mesh Ewald: An N-Log(N) method for Ewald Sums in large systems. *J. Chem. Phys.* **98**, 10089–10092 (1993).
92. Humphrey, W., Dalke, A. & Schulten, K. VMD: visual molecular dynamics. *J Mol Graph* **14**, 33–8, 27–8 (1996).

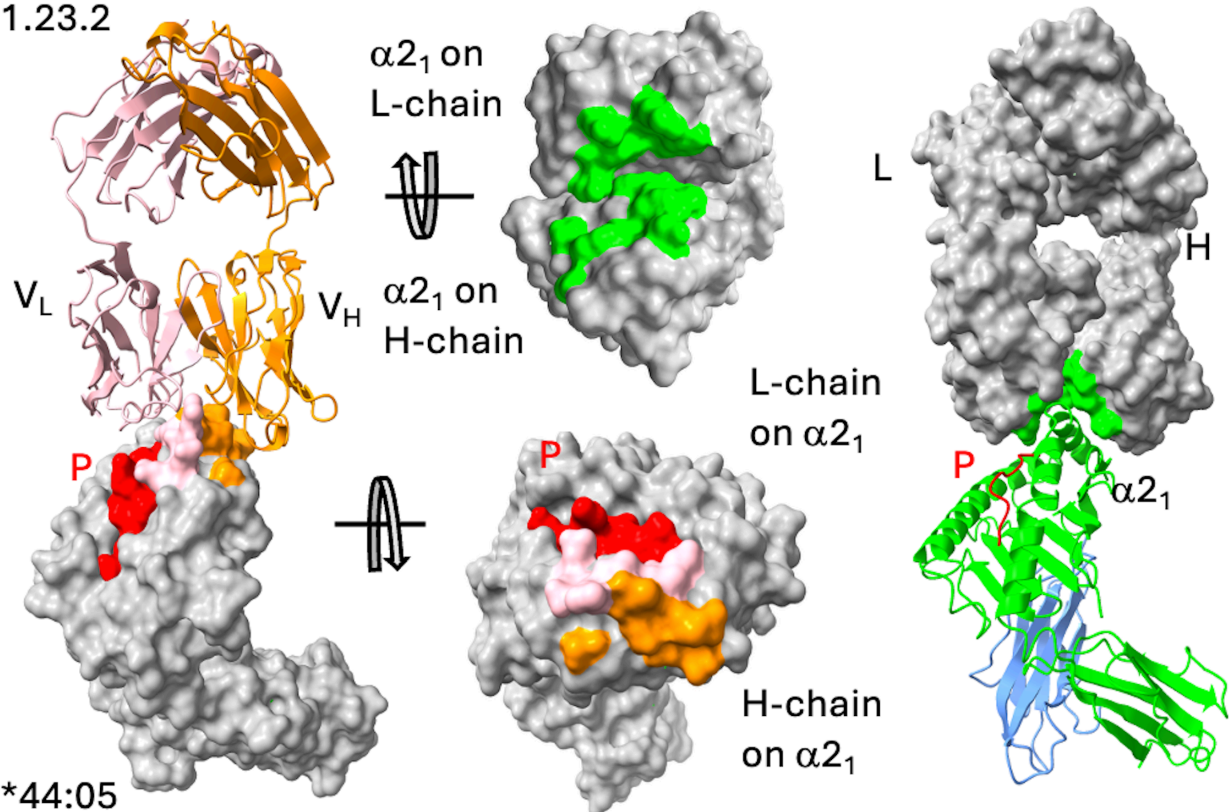
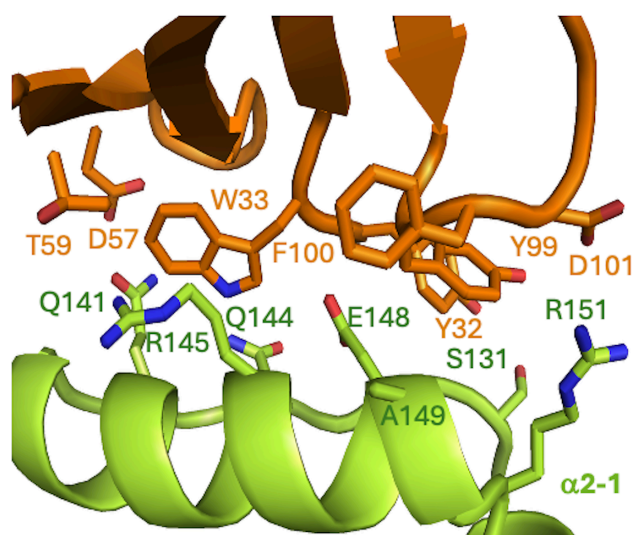
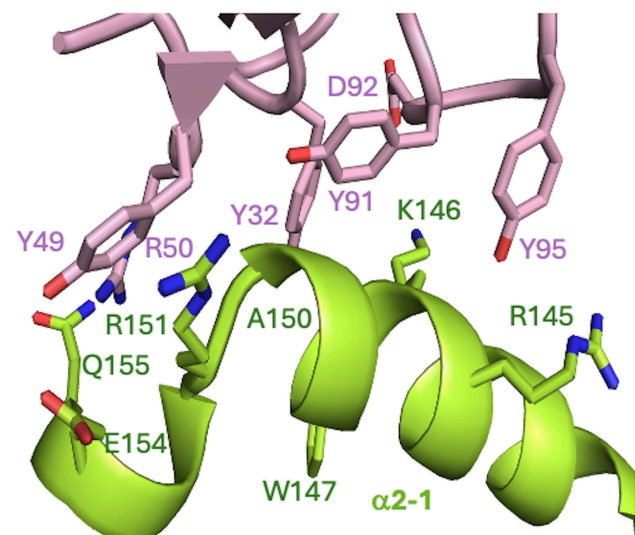
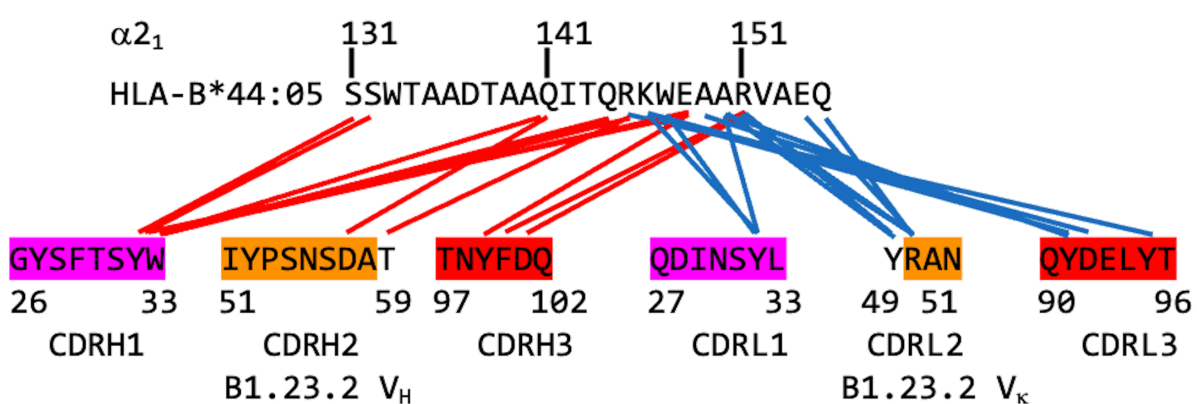
Editorial summary:

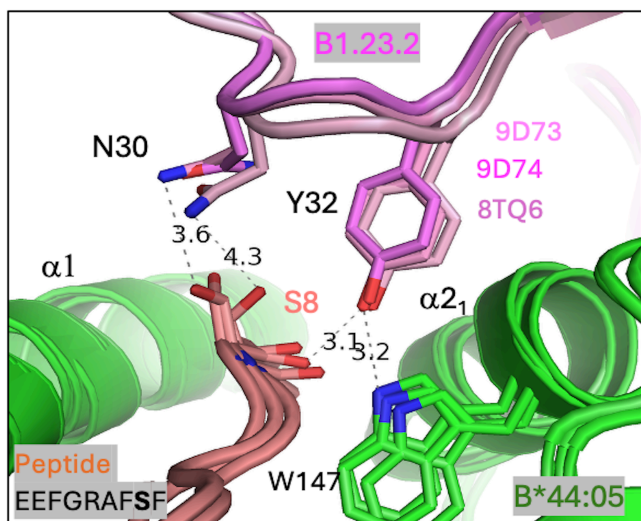
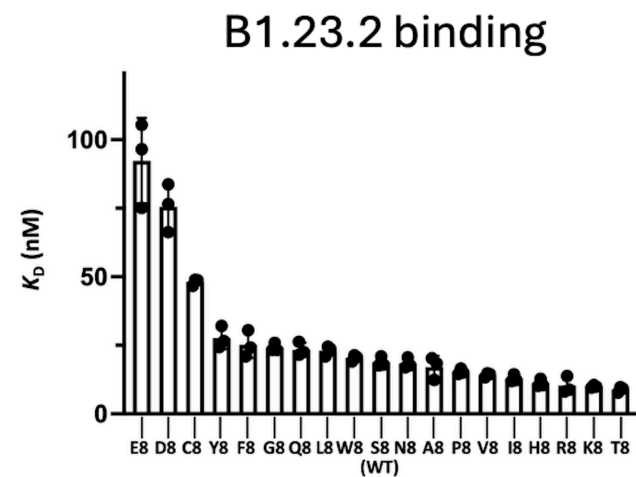
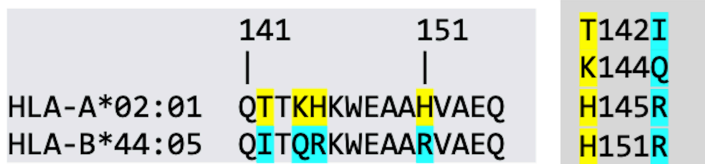
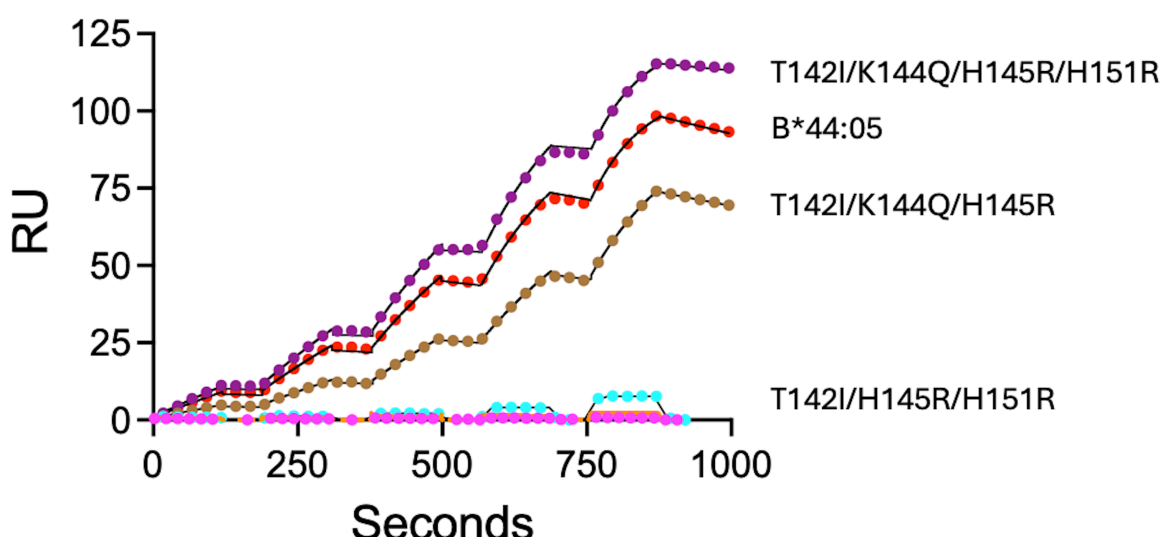
The B1.23.2 antibody binds HLA-B*44:05 at a site that overlaps the killer Ig-like receptor binding site. It blocks inhibitory receptor interactions, leads to NK cell activation and suppresses tumor growth in a humanized mouse model.

Peer review information:

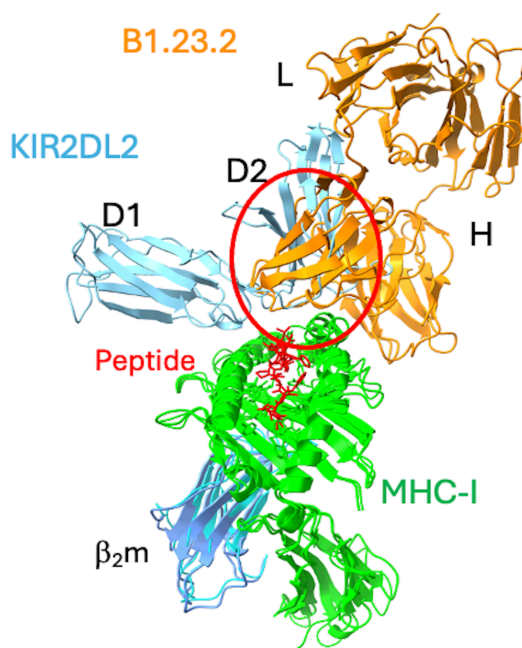
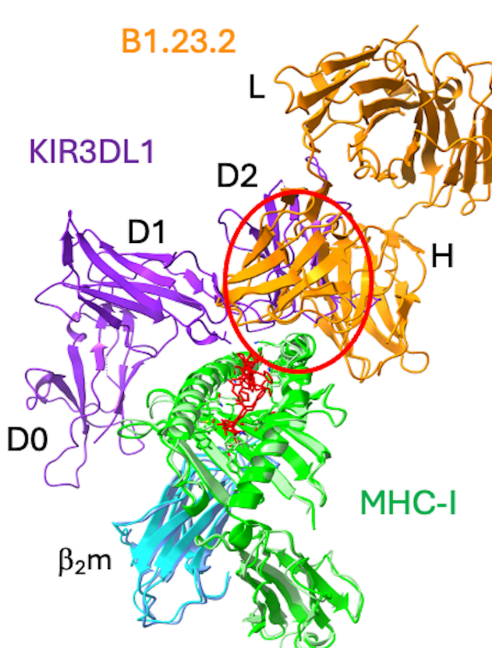
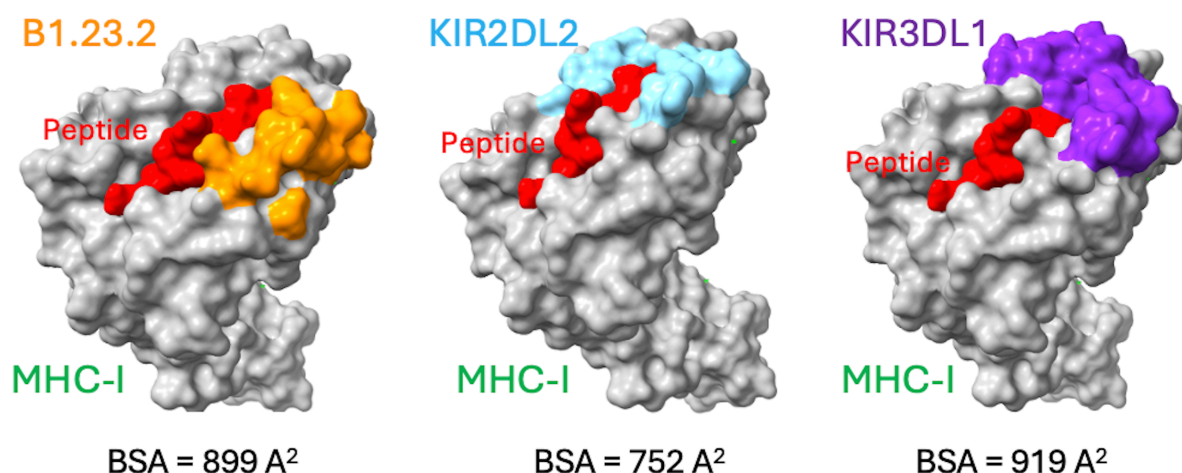
Communications Biology thanks Lawrence Stern, Efstratios Stratikos and the other, anonymous, reviewer(s) for their contribution to the peer review of this work. Primary Handling Editors: Huan Bao and Laura Rodríguez Pérez.

a HLA-B*44:05 binding to B1.23.2**b 2D Classification****c Best 2D class average****d Map****e Model****f Protocol****g Map resolution**

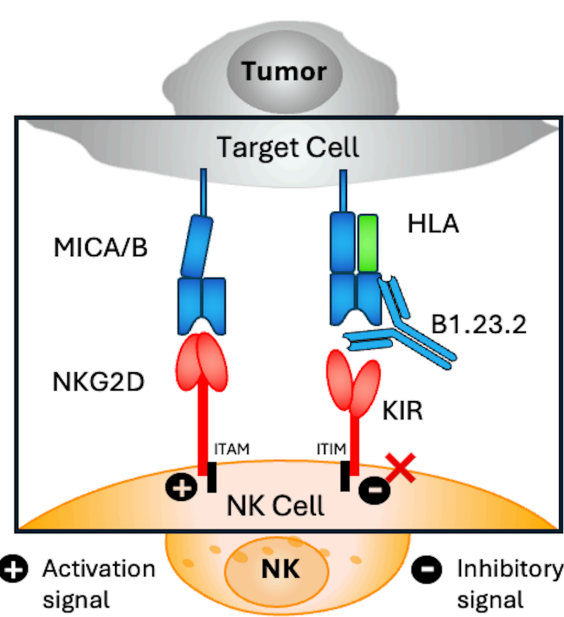
a B1.23.2**b** H-chain contacts with $\alpha 2_1$ L-chain contacts with $\alpha 2_1$ **c**

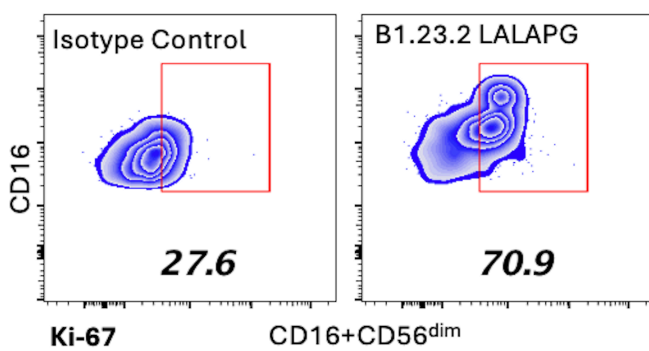
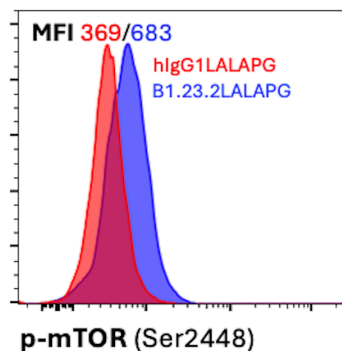
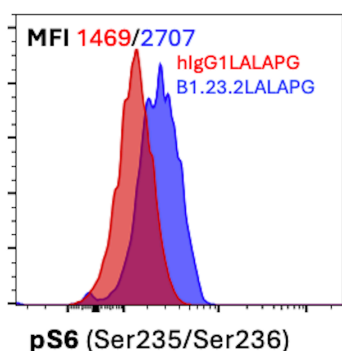
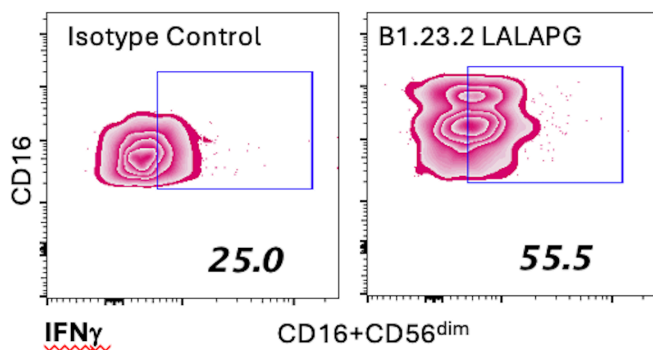
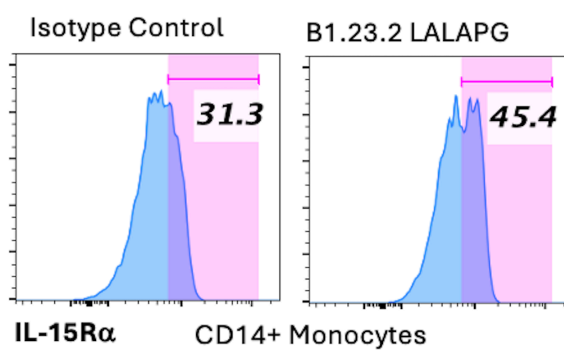
a**b****c****d****e**

	k_a ($M^{-1}s^{-1}$) ($\times 10^4$)	k_d (s^{-1}) ($\times 10^{-4}$)	K_D (μM)
A*02:01	ND	ND	ND
B*44:05	2.13 ± 0.01	4.7 ± 0.03	0.02 ± 0.0004
<i>A*02:01 mutants:</i>			
T142I/H145R	ND	ND	ND
T142I/H145R/H151R	poor fit	poor fit	weak binding, poor fit
T142I/K144Q/H145R	1.09 ± 0.04	5.02 ± 0.03	0.04 ± 0.002
T142I/K144Q/H145R/H151R	2.25 ± 0.07	1.59 ± 0.1	0.007 ± 0.0004

a B1.23.2 vs KIR2DL2**b B1.23.2 vs KIR3DL1****c Footprints on MHC-I****d Overlapping contacts on α₂1**

B*44:05	R145	K146	A149	A150	R151
B123-H	W33		Y99		D101
B123-H	T59				F100
B123-L	Y95	Y32	Y91	Y91	R50
B123-L		Y91		Y49	Y49
B123-L		D92		Y32	
C*03:01	R145	K146	A149	A150	R151
KIR2DL2	S133	Y105	S132	L104	E106
KIR2DL2	D135	F181	Y105		
KIR2DL2		D183	E106		
B*57:01	R145	K146	A149	A150	R151
KIR3DL1	S228	F276	E201	P199	E201
KIR3DL1	D230	Y200	S227	Y200	
KIR3DL1	F276	S279	F276		
KIR3DL1		E282			

e

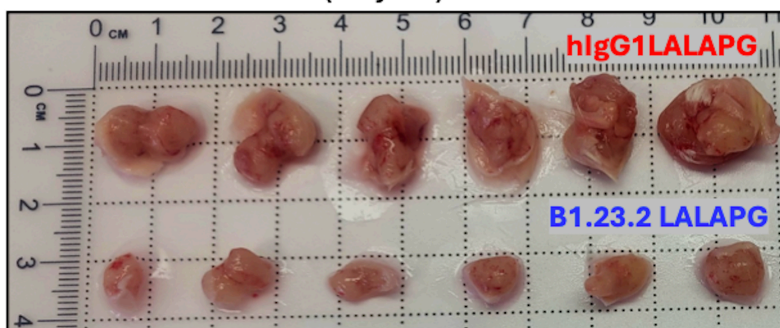
a**b****c****d****e****f**

KLM1 (human) Pancreatic cancer cells (s.c.) hIgG1LALAPG or B1.23.2 LALAPG (100ug, iv)

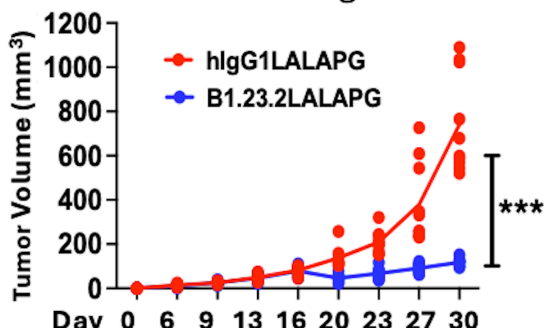
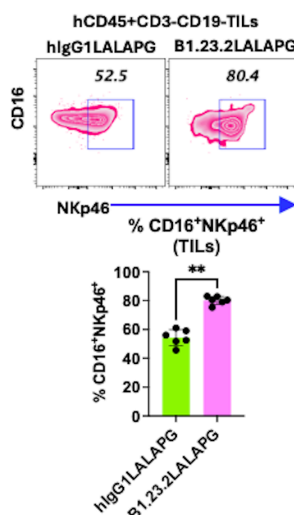


Grow in NSG IL-15 mice (engrafted 10⁶CD3⁺/mouse, i.v.) mAb treatment D16 to D27

KLM1 Tumor volume (Day 30)



KLM1 Tumor growth

**g****h**